Received: 22 October 2020 | Revised: 21 January 2021

DOI: 10.1111/sapm.12376

STUDIES IN APPLIED MATHEMATICS WILEY

ORIGINAL ARTICLE

On an averaged model for immiscible two-phase flow with surface tension and dynamic contact angle in a thin strip

Stephan B. Lunowa[1] | **Carina Bringedal**[2] | **Iuliu Sorin Pop**[1]

[1] Computational Mathematics, UHasselt – Hasselt University, Diepenbeek, Belgium

[2] Institute for Modelling Hydraulic and Environmental Systems, University of Stuttgart, Stuttgart, Germany

Correspondence
Stephan B. Lunowa, UHasselt – Hasselt University, Computational Mathematics, Agoralaan, 3590 Diepenbeek, Belgium.
Email: stephan.lunowa@uhasselt.be

Funding information
Universiteit Hasselt, Grant/Award Number: BOF17NI01; Deutsche Forschungsgemeinschaft, Grant/Award Number: 327154368; Fonds Wetenschappelijk Onderzoek, Grant/Award Numbers: G051418N, G0G1316M

Abstract

We consider a model for the flow of two immiscible fluids in a two-dimensional thin strip of varying width. This represents an idealization of a pore in a porous medium. The interface separating the fluids forms a freely moving interface in contact with the wall and is driven by the fluid flow and surface tension. The contact-line model incorporates Navier-slip boundary conditions and a dynamic and possibly hysteretic contact angle law. We assume a scale separation between the typical width and the length of the thin strip. Based on asymptotic expansions, we derive effective models for the two-phase flow. These models form a system of differential algebraic equations for the interface position and the total flux. The result is Darcy-type equations for the flow, combined with a capillary pressure–saturation relationship involving dynamic effects. Finally, we provide some numerical examples to show the effect of a varying wall width, of the viscosity ratio, of the slip boundary condition as well as of having a dynamic contact angle law.

KEYWORDS

asymptotic expansions, dynamic contact angle, freely moving interface, thin strip, two-phase flow, upscaled models

1 | INTRODUCTION

Many industrial and environmental processes, such as oil recovery, geological CO_2 sequestration, or groundwater pollution, strongly depend on the flow in the respective porous medium. In all these applications, it is necessary to describe the flow of all involved fluid phases at a macroscopic scale to allow for efficient simulations in large domains. In particular, the complex pore structure and the exact distribution of fluids are simplified into a representation by averaged quantities such as the porosity and saturation. The relations between these macroscopic quantities must be expressed with the help of effective parameters, which should combine all pore-scale effects. However, in many state-of-the-art models these parameters are postulated and not derived from a pore-scale model.

One of the earliest models for the macroscale flow in a porous medium was proposed by Darcy.[1] Based on column experiments for fully saturated, single-phase flow in a porous medium, a proportionality between the pressure gradient and the velocity was observed, involving the medium's permeability as proportionality factor. Subsequently, further experiments by Richards[2] and by Morrow and Harris[3] extended the theory to unsaturated and two-phase flow in porous media, respectively. The resulting flow models still include Darcy's law, with a then saturation-dependent permeability. However, they additionally involved the phase-pressure difference, also known as the capillary pressure, which appears due to surface tension between the phases.

Based on experiments at equilibrium conditions, nonlinear, but monotonic capillary pressure–saturation functions have been used for decades. However, already Morrow and Harris[3] showed that this relation also depends on the process—imbibition or drainage. Besides this hysteresis, further dynamic effects were reported in many experiments,[4–8] leading to a variety of nonmonotonic curves which cannot be combined into a simple capillary pressure–saturation function.

To overcome the mismatch between the experimental results and the mathematical models, several extensions of the capillary pressure–saturation relation have been proposed. Typically, dynamic effects and hysteresis are directly expressed in terms of spatial or temporal derivatives of the saturation leading to different capillary pressure models, for example, Refs. 9–12; for an overview, see Ref. 13. Alternatively, the interfacial area was introduced as an additional state variable leading to a capillary pressure–saturation-interfacial area relationship that implicitly models the dynamic and hysteretic effects via the change in interfacial area.[14,15] Other hysteresis models are based on the concept of percolating/nonpercolating phases.[16–18] These extended models are able to reproduce nonmonotonic phenomena such as saturation overshoot and fingering as shown in Refs. 19–21 by qualitative analysis using a traveling wave approach and in Refs. 22–27 by numerical simulations.

However, all models discussed above are considering the so-called Darcy scale, and thus describe the average behavior of the liquid phases disregarding the detailed pore structure and processes at the pore scale. It is crucial to understand the dependence of the effective parameters on the underlying pore structure. At the pore scale, the mathematical model can incorporate the detailed physical processes, but it is posed in the entire pore space, which is extremely complex, and needs to account for all interfaces between phases. Resolving the whole complicated pore space of realistic scenarios in direct numerical simulations is infeasible, so that further simplifications are necessary to link the properties of the different scales.

To approach this task, there exist a large variety of analytical upscaling techniques, see Ref. 28 for an overview. The volume averaging method has been used to derive effective equations for quantities at the level of a representative elementary volume, while restricting the form of constitutive equations using the second law of thermodynamics at the Darcy scale. This method has

been successfully applied to single-phase and two-phase flow in porous media in Refs. 29–31. However, the technique does only provide explicit expressions for the effective parameters in the constitutive equations via closure problems, when additional assumptions are made. Alternatively, the homogenization method is a (matched) asymptotic expansion approach for typically periodic systems, where there is a clear scale separation. The idea is to approximate the problem involving a small parameter ε (e.g., the ratio of an average pore diameter to a Darcy-scale length) by the limit problem and its solution as $\varepsilon \to 0$. For an introduction to this method, we mention Ref. 32 and the references therein. Many results for flow in porous media have been obtained by homogenization, see, for example, Refs. 33–39 leading either to explicit expressions or to so-called cell problems for the effective parameters. In both cases, knowledge of the underlying pore structure allows for the explicit computation of the effective parameters. Therefore, we apply the homogenization method to explicitly derive effective relations.

Here we consider a simplified geometry, namely, the flow through a single, long, and thin pore as a representative for the porous medium. Despite the very simplistic representation, the upscaling of thin-strip models typically leads to Darcy-scale models with the same structure as well-recognized Darcy-scale models in general porous media (see, e.g., Refs. 37–40). In addition, using a single pore allows for the explicit derivation of closed-form expressions for the upscaled quantities. We assume that the pore is filled by two incompressible and immiscible fluid phases. The interface separating the two fluids is traversal to the flow direction. The mathematical model consists of conservation laws for mass and momentum in time-dependent domains representing the fluids. Assuming a horizontal setting, we disregard gravity effects. The evolution of the interface separating the domains is not known a priori, but depends on the velocities of the fluids and on the surface tension between the fluids. Hence, the development of the boundary of the domains must be accounted for, and we have a free boundary problem.

While the fluid domains are assumed to be layered in Refs. 37–40, such that the fluid–fluid interface does not come into contact with the solid wall, we here consider the case when the interface is in contact with the pore walls. This requires a contact angle model, which is allowed to be dynamic or even hysteretic. In particular, this also implies that each fluid is only present either at the inlet or at the outlet. Note that the plug flow scenario considered in Ref. 40 has a similar fluid distribution, but the authors assume a fixed interface shape and a residual thin film, which yields dynamics that are very different from those generated by a variable interface with moving contact line. Furthermore, we allow for a slowly varying solid wall instead of a constant-width strip or tube used in Refs. 37–40.

Based on the discussed pore-scale model, we derive upscaled (Darcy-scale) models for two-phase or unsaturated single-phase flow in a porous medium under reasonable assumptions on the underlying physics. We follow the ideas in Refs. 37–39, where asymmetric expansions and transversal averaging is applied to obtain a macroscale model based on the simple, layered pore. We complement this with volume averages to account for the different geometry and fluid distribution. A similar strategy has been used to show that the upscaled models significantly differ for different flow regimes assuming stationary fluid–fluid interface shapes in Ref. 40, and in Ref. 39 when assuming a layered, parallel flow regime. In general, the thin-strip approach allows the derivation of explicit relations between the averaged quantities, while various additional features and processes can be easily incorporated (see, e.g., Refs. 39, 41–43).

This paper is organized as follows. In Section 2, we formulate the mathematical model for two-phase flow with evolving interface in a thin strip, which is then rescaled to obtain a nondimensional formulation. Next, we formally derive in Section 3 the effective models in the bulk domains and close to the interface when the ratio between the width and length of the thin strip approaches

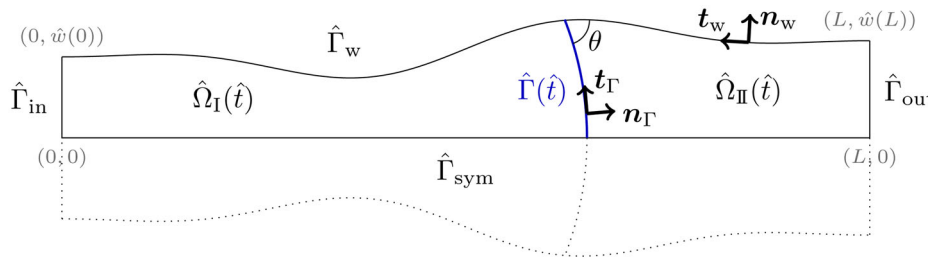

FIGURE 1 Sketch of the half thin strip $\hat{\Omega}$ filled by two fluids with interface $\hat{\Gamma}(\hat{t})$ at time $\hat{t}$

zero. These models form a system of differential algebraic equations for the interface position and the total flux. Based on the derived models, we discuss averaged and effective quantities and their relations in Section 4. In particular, there holds a Darcy-type equation for the flow and a capillary pressure–saturation relationship involving dynamic effects. Finally, Section 5 provides some numerical examples showing the behavior of the effective models for a constant as well as a varying wall width. The effect of the viscosity ratio, of the slip length, and of having a dynamic contact angle law is discussed in detail.

2 | MATHEMATICAL MODEL

We consider a two-dimensional thin strip of length $L > 0$, which is axisymmetric at $\hat{\Gamma}_{\mathrm{sym}} := [0, L] \times \{0\}$. Let $\hat{w} : [0, L] \to (0, \infty)$ be a given smooth function (which is bounded away from zero), that describes the wall $\hat{\Gamma}_{\mathrm{w}} := \{\hat{\boldsymbol{x}} \in (0, L) \times (0, \infty) \mid \hat{x}_2 = \hat{w}(\hat{x}_1)\}$. Here and in the following, the subscripts $\cdot_1$ and $\cdot_2$ denote the components of a vector. Then the domain of interest is $\hat{\Omega} := \{\hat{\boldsymbol{x}} \in (0, L) \times (0, \infty) \mid \hat{x}_2 < \hat{w}(\hat{x}_1)\}$. At each time $\hat{t} \in [0, \infty)$, the domain is partitioned into two subdomains $\hat{\Omega}_{\mathrm{I}}(\hat{t})$ and $\hat{\Omega}_{\mathrm{II}}(\hat{t})$, which represent the parts occupied by the two fluids; one at the inlet boundary $\hat{\Gamma}_{\mathrm{in}} := \{0\} \times [0, \hat{w}(0)]$ and the other at the outflow boundary $\hat{\Gamma}_{\mathrm{out}} := \{L\} \times [0, \hat{w}(L)]$. Figure 1 illustrates the geometry.

We consider the particular case when the two fluids are separated by an axisymmetric fluid–fluid interface $\hat{\Gamma}(\hat{t}) := \partial\hat{\Omega}_{\mathrm{I}}(\hat{t}) \cap \partial\hat{\Omega}_{\mathrm{II}}(\hat{t})$, which is in contact with the solid wall $\hat{\Gamma}_{\mathrm{w}}$. This interface has an a priori unknown location and shape, and therefore appears as a free boundary in the mathematical model. It is parameterized by $\hat{\boldsymbol{\gamma}} : [0, \infty) \times [0, 1] \to \overline{\hat{\Omega}}$, such that $\hat{\Gamma}(\hat{t}) = \{\hat{\boldsymbol{\gamma}}(\hat{t}, s) \mid s \in [0, 1]\}$. The parameterization starts at the symmetry boundary and ends at the wall, that is,

$$\hat{\gamma}_2(\hat{t}, 0) = 0, \qquad \hat{\gamma}_2(\hat{t}, 1) = \hat{w}(\hat{\gamma}_1(\hat{t}, 1)). \tag{1}$$

The point $\hat{\boldsymbol{x}}^*(\hat{t}) := \hat{\boldsymbol{\gamma}}(\hat{t}, 1)$ is the so-called contact point.

At all boundaries of $\hat{\Omega}$, the outward normal and tangential unit vectors are denoted $\boldsymbol{n}$ and $\boldsymbol{t}$ with an index specifying the part of the boundary, for example, $\boldsymbol{n}_{\mathrm{sym}}$ for the normal vector at the symmetry boundary $\hat{\Gamma}_{\mathrm{sym}}$. At the fluid–fluid interface $\hat{\Gamma}(\hat{t})$, the normal unit vector pointing from $\hat{\Omega}_{\mathrm{I}}(\hat{t})$ into $\hat{\Omega}_{\mathrm{II}}(\hat{t})$ is denoted by $\boldsymbol{n}_{\Gamma}$, while the tangential unit vector is $\boldsymbol{t}_{\Gamma}$. Therefore, these vectors are given by

$$\boldsymbol{t}_{\Gamma} = \frac{\partial_s \hat{\boldsymbol{\gamma}}}{|\partial_s \hat{\boldsymbol{\gamma}}|} = \frac{1}{\sqrt{(\partial_s \hat{\gamma}_1)^2 + (\partial_s \hat{\gamma}_2)^2}} \partial_s \hat{\boldsymbol{\gamma}} \qquad \boldsymbol{n}_{\Gamma} = \frac{\partial_s \boldsymbol{t}_{\Gamma}}{|\partial_s \boldsymbol{t}_{\Gamma}|} = \frac{1}{\sqrt{(\partial_s \hat{\gamma}_1)^2 + (\partial_s \hat{\gamma}_2)^2}} \begin{pmatrix} \partial_s \hat{\gamma}_2 \\ -\partial_s \hat{\gamma}_1 \end{pmatrix},$$

TABLE 1 Summary of all parameters (top), dimensionless numbers (center), and dimensional and dimensionless quantities and their respective scaling (bottom)

Parameter	Symbol	Dim.-less Number	Symbol	Value
Length of the thin strip	L	Scale ratio	ε	$\hat{w}(0)/L$
Characteristic velocity	U	Density ratio	R	$\rho_{\mathrm{II}}/\rho_{\mathrm{I}}$
Density of fluid m	ρ_m	Viscosity ratio	M	$\mu_{\mathrm{II}}/\mu_{\mathrm{I}}$
Viscosity of fluid m	μ_m	Reynolds number	Re	$\rho_{\mathrm{I}}UL/\mu_{\mathrm{I}}$
Surface tension coefficient	σ	Capillary number	Ca	$\mu_{\mathrm{I}}U/\sigma$
		Eff. capillary number	$\overline{\mathrm{Ca}}$	Ca/ε

Quantity	Dimensional	Dim.-less	Scaling	Inner expansion	Scaling
Position	$\hat{\boldsymbol{x}}$	$\boldsymbol{x}$	$[L, \varepsilon L]$	$\boldsymbol{X}$	$[\varepsilon L, \varepsilon L]$
Time	$\hat{t}$	t	$[L/U]$	t	$[L/U]$
Velocity of fluid m	$\hat{\boldsymbol{u}}_m$	$\boldsymbol{u}_m$	$[U]$	$\boldsymbol{U}_m$	$[U]$
Pressure of fluid m	$\hat{p}_m$	p_m	$[\mu_{\mathrm{I}}U/(\varepsilon^2 L)]$	P_m	$[\mu_{\mathrm{I}}U/(\varepsilon^2 L)]$
Interface parameterization	$\hat{\boldsymbol{\gamma}}$	$\boldsymbol{\gamma}$	$[L, \varepsilon L]$	$\boldsymbol{Y}$	$[\varepsilon L, \varepsilon L]$
Interface curvature	$\hat{\kappa}$	κ	$[1/L]$	K	$[1/L]$
Slip length	$\hat{\lambda}$	λ	$[\varepsilon L]$	λ	$[\varepsilon L]$
Wall function (width)	$\hat{w}$	w	$[\varepsilon L]$	w	$[\varepsilon L]$
Contact angle law	θ	θ	[1]	θ	[1]

$$\boldsymbol{t}_{\mathrm{w}} = -\frac{1}{\sqrt{1+(\partial_{\hat{x}_1}\hat{w})^2}}\begin{pmatrix}1\\ \partial_{\hat{x}_1}\hat{w}\end{pmatrix} \qquad \boldsymbol{n}_{\mathrm{w}} = \frac{1}{\sqrt{1+(\partial_{\hat{x}_1}\hat{w})^2}}\begin{pmatrix}-\partial_{\hat{x}_1}\hat{w}\\ 1\end{pmatrix},$$

$$\boldsymbol{t}_{\mathrm{sym}} = \begin{pmatrix}1\\0\end{pmatrix} \qquad \boldsymbol{n}_{\mathrm{sym}} = \begin{pmatrix}0\\-1\end{pmatrix},$$

$$\boldsymbol{t}_{\mathrm{in}} = \begin{pmatrix}0\\-1\end{pmatrix} \qquad \boldsymbol{n}_{\mathrm{in}} = \begin{pmatrix}-1\\0\end{pmatrix},$$

$$\boldsymbol{t}_{\mathrm{out}} = \begin{pmatrix}0\\1\end{pmatrix} \qquad \boldsymbol{n}_{\mathrm{out}} = \begin{pmatrix}1\\0\end{pmatrix}.$$

In each subdomain $\hat{\Omega}_m(\hat{t})$, $m \in \{\mathrm{I}, \mathrm{II}\}$, we assume that the flow is modeled by the incompressible Navier–Stokes equations, which are written in dimensional form

$$\rho_m\left(\partial_{\hat{t}}\hat{\boldsymbol{u}}_m + (\hat{\boldsymbol{u}}_m \cdot \hat{\nabla})\hat{\boldsymbol{u}}_m\right) + \hat{\nabla}\hat{p}_m = \mu_m\hat{\Delta}\hat{\boldsymbol{u}}_m \qquad \text{in } \hat{\Omega}_m(\hat{t}), \tag{2}$$

$$\hat{\nabla}\cdot\hat{\boldsymbol{u}}_m = 0 \qquad \text{in } \hat{\Omega}_m(\hat{t}), \tag{3}$$

where $\hat{\boldsymbol{u}}_m(\hat{t}, \hat{\boldsymbol{x}})$ and $\hat{p}_m(\hat{t}, \hat{\boldsymbol{x}})$ are the velocity and pressure of fluid m. The parameters ρ_m and μ_m denote the density and the dynamic viscosity of the fluid (Table 1 provides an overview of all parameters and quantities).

The symmetry conditions at $\hat{\Gamma}_{\mathrm{sym},m}(\hat{t}) := \hat{\Gamma}_{\mathrm{sym}} \cap \partial\hat{\Omega}_m(\hat{t})$ are

$$\hat{\boldsymbol{u}}_m \cdot \boldsymbol{n}_{\mathrm{sym}} = 0, \boldsymbol{t}_{\mathrm{sym}} \cdot \left(\hat{\nabla}\hat{\boldsymbol{u}}_m \boldsymbol{n}_{\mathrm{sym}} \right) = 0 \qquad \text{on } \hat{\Gamma}_{\mathrm{sym},m}(\hat{t}), \tag{4}$$

$$\hat{\nabla}\hat{p}_m \cdot \boldsymbol{n}_{\mathrm{sym}} = 0 \qquad \text{on } \hat{\Gamma}_{\mathrm{sym},m}(\hat{t}), \tag{5}$$

$$\boldsymbol{n}_\Gamma \cdot \boldsymbol{n}_{\mathrm{sym}} = 0 \qquad \text{at } s = 0. \tag{6}$$

The walls $\hat{\Gamma}_{\mathrm{w},m}(\hat{t}) := \hat{\Gamma}_{\mathrm{w}} \cap \partial\hat{\Omega}_m(\hat{t})$ in contact with fluid $m \in \{\mathrm{I}, \mathrm{II}\}$ are assumed impermeable, such that there is no fluid flow in normal direction, that is,

$$\hat{\boldsymbol{u}}_m \cdot \boldsymbol{n}_{\mathrm{w}} = 0 \qquad \text{on } \hat{\Gamma}_{\mathrm{w},m}(\hat{t}). \tag{7}$$

Traditionally, this is complemented with the no-slip condition $\hat{\boldsymbol{u}}_m \cdot \boldsymbol{t}_{\mathrm{w}} = 0$ under the assumption that the fluid adheres to the wall. However, the no-slip condition leads to a singularity in the pressure and in the shear stress at the contact point $\hat{\boldsymbol{x}}^*(t)$ between wall $\hat{\Gamma}_{\mathrm{w}}$ and interface $\hat{\Gamma}(\hat{t})$.[44–46] To overcome this issue, several alternative boundary conditions have been proposed for use close to the contact point (or contact line in three dimensions), see Refs. 47–49 and the references therein. Here, we consider the Navier-slip condition

$$\boldsymbol{t}_{\mathrm{w}} \cdot \left(\hat{\boldsymbol{u}}_m + 2\hat{\lambda}\hat{\mathbf{D}}(\hat{\boldsymbol{u}}_m)\boldsymbol{n}_{\mathrm{w}} \right) = 0 \qquad \text{on } \hat{\Gamma}_{\mathrm{w},m}(\hat{t}), \tag{8}$$

where $\hat{\mathbf{D}}(\hat{\boldsymbol{u}}) := (\hat{\nabla}\hat{\boldsymbol{u}} + (\hat{\nabla}\hat{\boldsymbol{u}})^T)/2$ denotes the symmetric strain and $\hat{\lambda}$ is the slip length. This condition has been proposed originally by Huh and Scriven[44] to resolve the contact-line problem, and has been frequently used.[50–55] Often, the Navier-slip condition is only applied close to the contact point. In this case, a variable slip length $\hat{\lambda}(\hat{x}_1)$ is adopted, decaying rapidly to zero away from the contact point $\hat{\boldsymbol{x}}^*(\hat{t})$ (see, e.g., Refs. 53, 56–58). This seems justified by molecular dynamics simulations showing that the no-slip boundary condition is only violated in a small region (up to some nm) around the contact point.[59–63] In addition, surface wettability and roughness strongly affect the slip behavior (see, e.g., Refs. 64–67 for a mathematical analysis).

Remark 1. To be general, we will consider two cases here: a constant slip length $\hat{\lambda}$ on the whole wall $\hat{\Gamma}_{\mathrm{w}}$, or a varying slip length $\hat{\lambda}(\hat{t}, \hat{x}_1) = \hat{\lambda}_e \exp(-c|\hat{x}_1 - \hat{x}_1^*(\hat{t})|)$ which decreases exponentially away from the contact point $\hat{\boldsymbol{x}}^*(\hat{t})$. Note that the overall dynamics of the two-phase system will be independent of the latter, local slip condition, and especially of the exact form used; only the flow field close to the interface will be affected (see Section 3). This is in accordance with the results in Refs. 46, 54. Furthermore, note that we consider for simplicity the same slip length $\hat{\lambda}$ for both fluids, although they could in principle differ. It is possible to extend the analysis below to incorporate fluid-dependent slip lengths.

At the contact point $\hat{\boldsymbol{x}}^*(t)$, the contact angle θ between the wall $\hat{\Gamma}_{\mathrm{w}}(\hat{t})$ and the fluid interface $\hat{\Gamma}(\hat{t})$ must be prescribed. Minimization of the total surface energy yields the well-known Young's relation $\sigma_{\mathrm{I}} - \sigma_{\mathrm{II}} = \sigma \cos\theta_s$, where σ_{I} and σ_{II} denote the surface tension coefficients between the solid and the two fluids, and σ the interfacial tension between the two fluids. The angle θ_s is called the static contact angle and measured from the side of fluid II, as shown in Figure 1. Experiments per-

formed under dynamic conditions show a dynamic behavior of the contact angle. This is expressed as an apparent contact angle θ, and has a major influence on the overall flow dynamics.[68] In general, observations show increasing advancing angles, but decreasing receding angles, when the contact-line velocity U increases.[46,69] The θ–U relation is essentially monotonic.

There are mainly two models to describe this phenomenon: the hydrodynamic theory and the molecular kinetic theory (for detailed reviews, see Refs. 48, 68, 70). The hydrodynamic theory emphasizes on dissipation due to viscous flow within the wedge of liquid near the moving contact line. The region close to the contact point is analyzed based on asymptotic expansions.[46,50,52,57,71,72] For two-phase flow, this yields the well-known Cox law $g(\theta) = g(\theta_s) + C\mu U/\sigma$ for the dynamic contact angle θ, where U denotes the contact-line velocity, the constant C depends on the specific slip model, and g is an analytically derived function, which can be approximated by $g(\theta) \approx \theta^3$ for small angles.[57] The other approach is the molecular kinetic theory, where the dissipation is described due to the dynamic friction associated with the moving contact line. This yields the relation $U = C_1 \sinh(C_2\sigma(\cos\theta_s - \cos\theta))$ with the constants C_1 and C_2 depending on molecular properties.[69,73,74] After linearization for small differences in the angles, one obtains $U = C\sigma(\cos\theta_s - \cos\theta)$ for some constant C.[68]

As for the slip length, the contact angle is strongly affected by surface wettability and roughness. In Refs. 68, 70, the resulting effects are made responsible for contact angle hysteresis, that is, that static contact angles can be achieved in the whole range $\theta_r < \theta_s < \theta_a$, where θ_a, θ_r denote the advancing and receding contact angles, respectively. Summarizing all the above results, we assume the contact angle θ to depend on the velocity $-\partial_t \hat{\boldsymbol{x}}^*(t) \cdot \boldsymbol{t}_{\mathrm{w}}$ of the contact point parallel to the wall. Recall that $\hat{\boldsymbol{x}}^* = \hat{\boldsymbol{\gamma}}|_{s=1}$, so this contact angle condition is expressed as

$$\cos(\theta(-\partial_t \hat{\boldsymbol{\gamma}} \cdot \boldsymbol{t}_{\mathrm{w}}|_{\hat{x}_1=\hat{\gamma}_1})) = \boldsymbol{t}_\Gamma \cdot \boldsymbol{t}_{\mathrm{w}}\big|_{\hat{x}_1=\hat{\gamma}_1} \qquad \text{at } s = 1, \tag{9}$$

where $\theta : \mathbb{R} \to (0, \pi)$ is a given dynamic contact angle model. Note that any dynamic contact angle model that satisfies assumption (A5) can be used. Specific relations for hysteretic θ and their effect on the behavior will be discussed in Subsection 3.4. Furthermore, to account for heterogeneities, the following analysis can be straightforwardly extended to the case when the contact angle also depends on the position $\hat{x}_1^*(t)$ of the contact point.

At the interface $\hat{\Gamma}(\hat{t})$, there holds continuity of the velocity and of the tangential stress, while the jump in the normal stress is caused by the surface tension

$$\hat{\boldsymbol{u}}_{\mathrm{I}} = \hat{\boldsymbol{u}}_{\mathrm{II}} \qquad \text{on } \hat{\Gamma}(\hat{t}), \tag{10}$$

$$-(\hat{p}_{\mathrm{I}} - \hat{p}_{\mathrm{II}})\boldsymbol{n}_\Gamma + 2\big(\mu_{\mathrm{I}}\hat{\mathbf{D}}(\hat{\boldsymbol{u}}_{\mathrm{I}}) - \mu_{\mathrm{II}}\hat{\mathbf{D}}(\hat{\boldsymbol{u}}_{\mathrm{II}})\big)\boldsymbol{n}_\Gamma = \sigma\hat{\kappa}\boldsymbol{n}_\Gamma \qquad \text{on } \hat{\Gamma}(\hat{t}), \tag{11}$$

where $\hat{\kappa} = \det(\partial_s \boldsymbol{\gamma}, \partial_s^2 \boldsymbol{\gamma})/|\partial_s \boldsymbol{\gamma}|^3$ is the local mean curvature of the interface. Note that this curvature generalizes to $\hat{\nabla} \cdot \boldsymbol{n}_\Gamma$ for three-dimensional domains. The interface moves according to the normal velocity of the fluids,

$$\partial_{\hat{t}} \hat{\boldsymbol{\gamma}} \cdot \boldsymbol{n}_\Gamma = \hat{\boldsymbol{u}}_{\mathrm{I}} \cdot \boldsymbol{n}_\Gamma \qquad \text{on } \hat{\Gamma}(\hat{t}). \tag{12}$$

At the inlet boundary $\hat{\Gamma}_{\mathrm{in}}$, either the pressure $\hat{p}_{\mathrm{in}}$ or the velocity $\hat{\boldsymbol{u}}$ in is given, namely, either

$$\hat{p}_{\mathrm{I}} = \hat{p}_{\mathrm{in}}, \quad \hat{\boldsymbol{u}}_{\mathrm{I}} \cdot \boldsymbol{t}_{\mathrm{in}} = 0 \qquad \text{or} \qquad \hat{\boldsymbol{u}}_{\mathrm{I}} = \hat{\boldsymbol{u}}_{\mathrm{in}} \qquad \text{on } \hat{\Gamma}_{\mathrm{in}}, \tag{13}$$

while an outflow boundary condition is applied at $\hat{\Gamma}_{\text{out}}$ (corresponding to $\hat{p}_{\text{out}} = 0$)

$$\hat{p}_{\text{II}} = 0, \quad \hat{\boldsymbol{u}}_{\text{II}} \cdot \boldsymbol{t}_{\text{out}} = 0 \qquad \text{on } \hat{\Gamma}_{\text{out}}. \tag{14}$$

The problem is closed by the initial conditions $\hat{\boldsymbol{\gamma}}|_{\hat{t}=0} = \hat{\boldsymbol{\gamma}}_0$ for the position of the interface $\hat{\Gamma}(0)$ and $\hat{\boldsymbol{u}}_m|_{\hat{t}=0} = \hat{\boldsymbol{u}}_{m,0}$ for the velocity in $\hat{\Omega}_m(0)$. In the following, we will omit the initial conditions and implicitly require them to match the asymptotic solutions in Section 3 to avoid possible initial layer solutions for small times.

2.1 | Dimensionless formulation

To quantify the importance of the different terms of the model, we rewrite the equations in a dimensionless form. As we consider a single, thin pore, we introduce the small parameter $\varepsilon = \hat{w}(0)/L \ll 1$ which characterizes the ratio of the typical width to the length of the thin strip. Note that in a general porous medium, ε would reflect the ratio of the size of a pore to the length scale of a representative elementary volume. With this, we rescale the governing equations using the dimensionless quantities(Table 1)

$$x_1 := \frac{\hat{x}_1}{L}, \quad x_2 := \frac{\hat{x}_2}{\hat{w}(0)} = \frac{\hat{x}_2}{\varepsilon L}, \quad t := \frac{\hat{t}U}{L}, \quad \lambda^\varepsilon := \frac{\hat{\lambda}}{\hat{w}(0)} = \frac{\hat{\lambda}}{\varepsilon L},$$

$$\gamma_1^\varepsilon(t,s) := \frac{\hat{\gamma}_1(\hat{t},s)}{L}, \quad \gamma_2^\varepsilon(t,s) := \frac{\hat{\gamma}_2(\hat{t},s)}{\hat{w}(0)} = \frac{\hat{\gamma}_2(\hat{t},s)}{\varepsilon L}, \quad w^\varepsilon(x_1) := \frac{\hat{w}(\hat{x}_1)}{\hat{w}(0)} = \frac{\hat{w}(\hat{x}_1)}{\varepsilon L},$$

$$\theta^\varepsilon(u) := \theta(uU), \quad \boldsymbol{u}_m^\varepsilon(t,\boldsymbol{x}) := \frac{\hat{\boldsymbol{u}}_m(\hat{t},\hat{\boldsymbol{x}})}{U}, \quad p_m^\varepsilon(t,\boldsymbol{x}) := \frac{\hat{p}_m(\hat{t},\hat{\boldsymbol{x}})\varepsilon^2 L}{\mu_{\text{I}} U},$$

where $U > 0$ denotes a characteristic velocity. In particular, the pressure reference $\mu_{\text{I}}U/(\varepsilon^2 L)$ is chosen such that pressure and viscous stress terms in Equation (2) are balanced. For moderate Reynolds number, this choice ensures laminar flow driven by the pressure gradients, which is crucial for the validity of Darcy's law on the Darcy scale. Note that the coordinates x_1 and x_2 are scaled differently to obtain a domain of order 1, $\mathcal{O}(\varepsilon^0)$. Hence, the nondimensional differential operators are

$$\nabla^\varepsilon = \begin{pmatrix} \partial_{x_1} \\ \varepsilon^{-1}\partial_{x_2} \end{pmatrix}, \qquad \Delta^\varepsilon = \partial_{x_1}^2 + \varepsilon^{-2}\partial_{x_2}^2,$$

and the divergence changes accordingly. The nondimensional domains and boundaries become

$$\Gamma^\varepsilon(t) = \{\boldsymbol{\gamma}^\varepsilon(t,s) \mid s \in [0,1]\}, \quad \Omega^\varepsilon = \{\boldsymbol{x} \in (0,1)\times(0,\infty) \mid x_2 < w^\varepsilon(x_1)\},$$

$$\Gamma_{\text{in}}^\varepsilon = \{0\}\times[0,1], \quad \mathcal{M} := \{O \subset \Omega^\varepsilon \setminus \Gamma^\varepsilon(t) \mid O \cup \Gamma_{\text{in}}^\varepsilon \text{ is connected}\},$$

$$\Omega_{\text{I}}^\varepsilon(t) = \bigcup_{O\in\mathcal{M}} O, \quad \Omega_{\text{II}}^\varepsilon(t) = \Omega^\varepsilon \setminus (\Gamma^\varepsilon(t) \cup \Omega_{\text{I}}^\varepsilon(t)), \quad \Gamma_{\text{out}}^\varepsilon = \{1\}\times[0,w^\varepsilon(1)],$$

$$\Gamma_{\text{sym},m}^\varepsilon(t) = \{\boldsymbol{x} \in \partial\Omega_m^\varepsilon(t) \mid x_2 = 0\}, \quad \Gamma_{\text{w},m}^\varepsilon(t) = \{\boldsymbol{x} \in \partial\Omega_m^\varepsilon(t) \mid x_2 = w^\varepsilon(x_1)\}.$$

After the rescaling of Equations (1–14), the dimensionless equations read

$$\varepsilon^2 \mathrm{Re}\left(\partial_t \boldsymbol{u}_{\mathrm{I}}^\varepsilon + (\boldsymbol{u}_{\mathrm{I}}^\varepsilon \cdot \nabla^\varepsilon)\boldsymbol{u}_{\mathrm{I}}^\varepsilon\right) + \nabla^\varepsilon p_{\mathrm{I}}^\varepsilon = \varepsilon^2 \Delta^\varepsilon \boldsymbol{u}_{\mathrm{I}}^\varepsilon \quad \text{in } \Omega_{\mathrm{I}}^\varepsilon(t), \tag{15}$$

$$\varepsilon^2 \mathrm{RRe}\left(\partial_t \boldsymbol{u}_{\mathrm{II}}^\varepsilon + (\boldsymbol{u}_{\mathrm{II}}^\varepsilon \cdot \nabla^\varepsilon)\boldsymbol{u}_{\mathrm{II}}^\varepsilon\right) + \nabla^\varepsilon p_{\mathrm{II}}^\varepsilon = \mathrm{M}\varepsilon^2 \Delta^\varepsilon \boldsymbol{u}_{\mathrm{II}}^\varepsilon \quad \text{in } \Omega_{\mathrm{II}}^\varepsilon(t), \tag{16}$$

$$\nabla^\varepsilon \cdot \boldsymbol{u}_m^\varepsilon = 0 \quad \text{in } \Omega_m^\varepsilon(t), \tag{17}$$

$$\boldsymbol{u}_m^\varepsilon \cdot \boldsymbol{n}_{\mathrm{sym}} = 0, \quad \boldsymbol{t}_{\mathrm{sym}} \cdot \left(\nabla^\varepsilon \boldsymbol{u}_m^\varepsilon \boldsymbol{n}_{\mathrm{sym}}\right) = 0 \quad \text{on } \Gamma_{\mathrm{sym},m}^\varepsilon(t), \tag{18}$$

$$\nabla^\varepsilon p_m^\varepsilon \cdot \boldsymbol{n}_{\mathrm{sym}} = 0, \quad \text{on } \Gamma_{\mathrm{sym},m}^\varepsilon(t), \tag{19}$$

$$\text{either} \quad p_{\mathrm{I}}^\varepsilon = p_{\mathrm{in}}^\varepsilon, \quad \boldsymbol{u}_{\mathrm{I}}^\varepsilon \cdot \boldsymbol{t}_{\mathrm{in}} = 0, \qquad \text{or} \qquad \boldsymbol{u}_{\mathrm{I}}^\varepsilon = \boldsymbol{u}_{\mathrm{in}}^\varepsilon \quad \text{on } \Gamma_{\mathrm{in}}^\varepsilon, \tag{20}$$

$$p_{\mathrm{II}}^\varepsilon = 0, \quad \boldsymbol{u}_{\mathrm{II}}^\varepsilon \cdot \boldsymbol{t}_{\mathrm{out}} = 0 \quad \text{on } \Gamma_{\mathrm{out}}^\varepsilon, \tag{21}$$

$$\boldsymbol{t}_{\mathrm{w}}^\varepsilon \cdot (\boldsymbol{u}_m^\varepsilon + 2\varepsilon\lambda^\varepsilon \mathbf{D}^\varepsilon(\boldsymbol{u}_m^\varepsilon)\boldsymbol{n}_{\mathrm{w}}^\varepsilon) = 0, \quad \boldsymbol{u}_m^\varepsilon \cdot \boldsymbol{n}_{\mathrm{w}}^\varepsilon = 0 \quad \text{on } \Gamma_{\mathrm{w},m}^\varepsilon(t), \tag{22}$$

$$\partial_t \begin{pmatrix} \gamma_1^\varepsilon \\ \varepsilon\gamma_2^\varepsilon \end{pmatrix} \cdot \boldsymbol{n}_\Gamma^\varepsilon = \boldsymbol{u}_{\mathrm{I}}^\varepsilon \cdot \boldsymbol{n}_\Gamma^\varepsilon, \quad \boldsymbol{u}_{\mathrm{I}}^\varepsilon = \boldsymbol{u}_{\mathrm{II}}^\varepsilon \quad \text{on } \Gamma^\varepsilon(t), \tag{23}$$

$$-(p_{\mathrm{I}}^\varepsilon - p_{\mathrm{II}}^\varepsilon)\boldsymbol{n}_\Gamma^\varepsilon + 2\varepsilon^2\left(\mathbf{D}^\varepsilon(\boldsymbol{u}_{\mathrm{I}}^\varepsilon) - \mathrm{M}\mathbf{D}^\varepsilon(\boldsymbol{u}_{\mathrm{II}}^\varepsilon)\right)\boldsymbol{n}_\Gamma^\varepsilon = \frac{\varepsilon^2}{\mathrm{Ca}}\kappa^\varepsilon \boldsymbol{n}_\Gamma^\varepsilon \quad \text{on } \Gamma^\varepsilon(t), \tag{24}$$

$$\boldsymbol{n}_\Gamma^\varepsilon \cdot \boldsymbol{n}_{\mathrm{sym}} = 0 \quad \text{at } s = 0, \tag{25}$$

$$\cos(\theta^\varepsilon(-\partial_t \boldsymbol{\gamma}^\varepsilon \cdot \boldsymbol{t}_{\mathrm{w}}^\varepsilon|_{x_1=\gamma_1^\varepsilon})) = \boldsymbol{t}_\Gamma^\varepsilon \cdot \boldsymbol{t}_{\mathrm{w}}^\varepsilon\big|_{x_1=\gamma_1^\varepsilon} \quad \text{at } s = 1, \tag{26}$$

for $m \in \{\mathrm{I}, \mathrm{II}\}$, where the dimensionless numbers R, M, Re, and Ca are given in Table 1. The nondimensional strain is given by $\mathbf{D}^\varepsilon(\boldsymbol{u}^\varepsilon) = (\nabla^\varepsilon \boldsymbol{u}^\varepsilon + (\nabla^\varepsilon \boldsymbol{u}^\varepsilon)^T)/2$ and the transformed normal and tangential vectors are

$$\boldsymbol{t}_{\mathrm{w}}^\varepsilon = -\frac{1}{\sqrt{1+\varepsilon^2(\partial_{x_1} w^\varepsilon)^2}}\begin{pmatrix} 1 \\ \varepsilon\partial_{x_1} w^\varepsilon \end{pmatrix}, \qquad \boldsymbol{n}_{\mathrm{w}}^\varepsilon = \frac{1}{\sqrt{1+\varepsilon^2(\partial_{x_1} w^\varepsilon)^2}}\begin{pmatrix} -\varepsilon\partial_{x_1} w^\varepsilon \\ 1 \end{pmatrix},$$

$$\boldsymbol{t}_\Gamma^\varepsilon = \frac{1}{\sqrt{(\partial_s\gamma_1^\varepsilon)^2 + \varepsilon^2(\partial_s\gamma_2^\varepsilon)^2}}\begin{pmatrix} \partial_s\gamma_1^\varepsilon \\ \varepsilon\partial_s\gamma_2^\varepsilon \end{pmatrix}, \qquad \boldsymbol{n}_\Gamma^\varepsilon = \frac{1}{\sqrt{(\partial_s\gamma_1^\varepsilon)^2 + \varepsilon^2(\partial_s\gamma_2^\varepsilon)^2}}\begin{pmatrix} \varepsilon\partial_s\gamma_2^\varepsilon \\ -\partial_s\gamma_1^\varepsilon \end{pmatrix}.$$

Furthermore, the nondimensional curvature is given by

$$\kappa^\varepsilon = \frac{\varepsilon \det(\partial_s \boldsymbol{\gamma}^\varepsilon, \partial_s^2 \boldsymbol{\gamma}^\varepsilon)}{\left((\partial_s \gamma_1^\varepsilon)^2 + \varepsilon^2 (\partial_s \gamma_2^\varepsilon)^2\right)^{3/2}} = \frac{\varepsilon\left(\partial_s \gamma_1^\varepsilon \partial_s^2 \gamma_2^\varepsilon - \partial_s \gamma_2^\varepsilon \partial_s^2 \gamma_1^\varepsilon\right)}{\left((\partial_s \gamma_1^\varepsilon)^2 + \varepsilon^2 (\partial_s \gamma_2^\varepsilon)^2\right)^{3/2}}.$$

Remark 2. Integrating Equation (17) for $m = \mathrm{I}$ over $V_a = \{\boldsymbol{x} \in \Omega_\mathrm{I}^\varepsilon(t) \mid x_1 < a\}$ for any $a < \min_{s\in[0,1]} \gamma_1^\varepsilon(t,s)$ yields by the Gauss theorem and the boundary conditions Equations (18–22)

$$0 = \int_{V_a} \nabla^\varepsilon \cdot \boldsymbol{u}_\mathrm{I}^\varepsilon d\boldsymbol{x} = \int_{\partial V_a} \boldsymbol{u}_\mathrm{I}^\varepsilon \cdot \boldsymbol{n} ds = \int_0^{w^\varepsilon(a)} u_{\mathrm{I},1}^\varepsilon|_{x_1=a} dx_2 - \int_0^1 u_{\mathrm{I},1}^\varepsilon|_{x_1=0} dx_2.$$

Denoting the total flux into the half strip by $q^\varepsilon(t,0) := \int_0^1 u_{\mathrm{I},1}^\varepsilon(t,\boldsymbol{x})|_{x_1=0} dx_2$, we obtain that for all $a < \min_{s\in[0,1]} \gamma_1^\varepsilon(t,s)$ the total flux $q^\varepsilon(t,a) := \int_0^{w^\varepsilon(a)} u_{\mathrm{I},1}^\varepsilon|_{x_1=a} dx_2 = q^\varepsilon(t,0)$. Analogously, integrating Equation (17) for $m = \mathrm{I}$ over $\Omega_\mathrm{I}^\varepsilon(t)$ and for $m = \mathrm{II}$ over $V_a = \{\boldsymbol{x} \in \Omega_\mathrm{II}^\varepsilon \mid x_1 < a\}$ for any $a > \max_{s\in[0,1]} \gamma_1^\varepsilon(t,s)$ yields by the Gauss theorem, the boundary conditions, Equations (18–22), and the continuity of velocity at the interface, Equation (23), that

$$0 = \int_{\Omega_\mathrm{I}^\varepsilon} \nabla^\varepsilon \cdot \boldsymbol{u}_\mathrm{I}^\varepsilon d\boldsymbol{x} + \int_{V_a} \nabla^\varepsilon \cdot \boldsymbol{u}_\mathrm{II}^\varepsilon d\boldsymbol{x} = -q^\varepsilon(t,0) + \int_0^{w^\varepsilon(a)} u_{\mathrm{II},1}^\varepsilon|_{x_1=a} dx_2,$$

that is, the total flux $q(t,a) := \int_0^{w^\varepsilon(a)} u_{\mathrm{II},1}^\varepsilon|_{x_1=a} dx_2 = q^\varepsilon(t,0)$ for all $a > \max_{s\in[0,1]} \gamma_1^\varepsilon(t,s)$. Within the interval $[\min_{s\in[0,1]} \gamma_1^\varepsilon(t,s), \max_{s\in[0,1]} \gamma_1^\varepsilon(t,s)]$, the same calculation shows that the sum of the two fluxes over the respective parts of the domain equals the total flux $q^\varepsilon(t,0)$. This means that the total flux is independent of x_1, so we will simply use $q^\varepsilon(t)$ in this result for the subsequent analysis.

3 | ASYMPTOTIC EXPANSIONS

In this section, we derive the formal solution for the two-phase flow system Equations (15-26) in the asymptotic limit as $\varepsilon \to 0$, that is, the behavior in the limit when the thin strip becomes infinitely thin. We start with the solution in the bulk domains $\Omega_m^\varepsilon(t)$, $m \in \{\mathrm{I}, \mathrm{II}\}$, away from the interface $\Gamma^\varepsilon(t)$, where either fluid I or II is present, respectively. In the subsequent section, we show that these bulk solutions are connected via a boundary layer solution in the vicinity of $\Gamma^\varepsilon(t)$. Altogether, the solution is of Hagen–Poiseuille type in the bulk coupled by a dynamic Young–Laplace law at the interface, such that the interface position and the total flux are given by differential algebraic equations. Furthermore, we show that the solution for vanishing viscosity ratio $\mathrm{M} \to 0$ matches the asymptotic limit for unsaturated one-phase flow. Finally, a reformulation for hysteretic contact angle models is discussed.

For the following analysis, we use an asymptotic expansion technique with respect to ε to derive effective models. All variables are assumed to be smooth and to depend regularly on ε starting with the leading order $\mathcal{O}(\varepsilon^0)$. We apply the homogenization ansatz

$$\boldsymbol{u}_m^\varepsilon(t,\boldsymbol{x}) = \boldsymbol{u}_m^0(t,\boldsymbol{x}) + \varepsilon \boldsymbol{u}_m^1(t,\boldsymbol{x}) + \mathcal{O}(\varepsilon^2),$$

$$p_m^\varepsilon(t,\boldsymbol{x}) = p_m^0(t,\boldsymbol{x}) + \varepsilon p_m^1(t,\boldsymbol{x}) + \mathcal{O}(\varepsilon^2),$$

$$\boldsymbol{\gamma}^\varepsilon(t,s) = \boldsymbol{\gamma}^0(t,s) + \varepsilon \boldsymbol{\gamma}^1(t,s) + \mathcal{O}(\varepsilon^2)$$

for $m \in \{\mathrm{I}, \mathrm{II}\}$. Inserting the asymptotic expansions into the two-phase flow equations Equations (15–26) and equating terms of the same order in ε, we will obtain the asymptotic equations and solutions in the limit as $\varepsilon \to 0$. To this end, we need some assumptions on the parameters of the model.

(A1) The Reynolds number Re and its product with the density ratio R are uniformly bounded for all $0 < \varepsilon \ll 1$, that is, there exists $C \in (0,\infty)$ such that $\mathrm{Re} \le C$ and $\mathrm{RRe} \le C$ independent of ε. In other words, $\mathrm{Re} = \mathcal{O}(\varepsilon^0)$ or $\mathrm{Re} = \mathrm{o}(\varepsilon^0)$, and $\mathrm{RRe} = \mathcal{O}(\varepsilon^0)$ or $\mathrm{RRe} = \mathrm{o}(\varepsilon^0)$.

(A2) The viscosity ratio M of the fluids is of order 1, $\mathrm{M} = \mathcal{O}(\varepsilon^0)$.

(A3) According to Remark 1, the slip length λ^ε has the form

$$\lambda^\varepsilon(t,x_1) = \lambda^0 + \lambda_e \exp\left(-\frac{|x_1 - x_1^*(t)|}{\varepsilon}\right)$$

for given constants $\lambda^0, \lambda_e \ge 0$ that are independent of ε. Moreover, there holds either $\lambda_e = 0$, or $\lambda^0 = 0$. Note that the latter represents the case of rapidly decaying slip away from the interface, so that λ^ε has the expansion $\lambda^\varepsilon(t,x_1) = \mathcal{O}(\varepsilon^N)$ for arbitrary $N \in \mathbb{N}$ as long as $x_1 - x_1^*(t) \gg \varepsilon$.

(A4) The wall function w^ε has a uniform expansion

$$w^\varepsilon(x_1) = w^0(x_1) + \varepsilon w^1(x_1) + \mathcal{O}(\varepsilon^2),$$

where w^ε, $w^0 : [0,1] \to (0,\infty)$ are continuously differentiable (and thus bounded away from zero). Moreover, there holds $w^0(0) = 1$ and $\partial_{x_1} w^0(0) = \partial_{x_1} w^0(1) = 0$.

(A5) The contact angle relation θ^ε has a uniform expansion

$$\theta^\varepsilon(u) = \theta^0(u) + \varepsilon\theta^1(u) + \mathcal{O}(\varepsilon^2),$$

where $\theta^0 : \mathbb{R} \to (0,\pi)$ is Lipschitz-continuous.

(A6) If the velocity boundary condition $\boldsymbol{u}_\mathrm{I}^\varepsilon = \boldsymbol{u}_\mathrm{in}^\varepsilon$ is used at the inlet $\Gamma_\mathrm{in}^\varepsilon$, the velocity is given by

$$\boldsymbol{u}_\mathrm{in}^\varepsilon(t,\boldsymbol{x}) = \begin{pmatrix} 3q(t)\frac{(1+2\lambda^0)-x_2^2}{6\lambda^0+2} + \mathcal{O}(\varepsilon) \\ \mathcal{O}(\varepsilon^2) \end{pmatrix},$$

where $q : [0,\infty) \to \mathbb{R}$ is a continuous function independent of ε.

As will be seen below, (A1) ensures that the flow remains laminar. Furthermore, (A2) restricts the discussion to moderately viscous liquids. While $\mathrm{M} \gg 1$ would result in a highly viscous second fluid which gets immobile as $\varepsilon \to 0$, we will discuss the case $\mathrm{M} \ll 1$ of a extremely mobile fluid such as air (compared to water or oil) separately in Subsection 3.3. The asymptotic expansions stated in (A4) and (A5) are crucial for the derivation. As discussed in Section 2, slip is necessary to allow the movement of the contact point. Hence, (A3) requires a simple expression of the slip at

the pore walls close to the interface to avoid technical complexity, while allowing for the typical no-slip condition at the pore walls away from the interface ($\lambda^0 = 0$). The case of global slip conditions ($\lambda^0 > 0$) generalizes this to applications where the slip length is of the same order as the diameter, for example, in nanofluidic devices or for fluids with low viscosity. The assumption of a horizontal wall at the inlet and at the outlet ($\partial_{x_1} w^0(0) = \partial_{x_1} w^0(1) = 0$) in (A4) is used to exclude possible boundary-layer effects caused by nonmatching boundary conditions. The inlet velocity in (A6) is then the Hagen–Poiseuille profile incorporating the Navier-slip condition. Assumptions (A4) and (A6) can be relaxed if the boundary conditions at $\Gamma^\varepsilon_{\text{in}}$ and $\Gamma^\varepsilon_{\text{out}}$, Equations (20–21), are replaced appropriately, or if the resulting boundary layer matches the asymptotic solution of the following analysis. We observe that (A4) rules out the possibility that the pore has walls with rapidly oscillatory characteristics (so-called "rough walls"). Such walls can be characterized by a function $w^\varepsilon(x_1) = w^0(x_1) + \varepsilon w^1(x_1/\varepsilon) + \mathcal{O}(\varepsilon)$. Clearly, this would strongly affect the shape and position of the interface. A naive extension of the following results would yield unphysical oscillations of the interface, so that we restrict the discussion to slowly varying walls.

Note that the normal and tangential vectors $\boldsymbol{n}^\varepsilon_\Gamma$, $\boldsymbol{t}^\varepsilon_\Gamma$, $\boldsymbol{n}^\varepsilon_{\text{w}}$, and $\boldsymbol{t}^\varepsilon_{\text{w}}$ depend on $\boldsymbol{\gamma}^\varepsilon$ and w^ε, respectively, such that these can be expanded, for example,

$$\boldsymbol{n}^\varepsilon_{\text{w}} = \begin{pmatrix} 0 \\ 1 \end{pmatrix} - \varepsilon \begin{pmatrix} \partial_{x_1} w^0 \\ 0 \end{pmatrix} + \mathcal{O}(\varepsilon^2), \tag{27}$$

$$\boldsymbol{n}^\varepsilon_\Gamma = \begin{cases} \begin{pmatrix} 0 \\ -\text{sign}(\partial_s \gamma_1^0) \end{pmatrix} + \varepsilon \frac{1}{|\partial_s \gamma_1^0|} \begin{pmatrix} \partial_s \gamma_2^0 \\ -\partial_s \gamma_1^1 \end{pmatrix} + \mathcal{O}(\varepsilon^2) & \text{for } \partial_s \gamma_1^0 \neq 0, \\ \frac{1}{\sqrt{(\partial_s \gamma_1^1)^2 + (\partial_s \gamma_2^0)^2}} \begin{pmatrix} \partial_s \gamma_2^0 \\ -\partial_s \gamma_1^1 \end{pmatrix} + \varepsilon \frac{1}{\sqrt{(\partial_s \gamma_1^1)^2 + (\partial_s \gamma_2^0)^2}} \begin{pmatrix} \partial_s \gamma_2^1 \\ -\partial_s \gamma_1^2 \end{pmatrix} & \\ \quad + \varepsilon \frac{\partial_s \gamma_1^1 \partial_s \gamma_1^2 + \partial_s \gamma_2^0 \partial_s \gamma_2^1}{((\partial_s \gamma_1^1)^2 + (\partial_s \gamma_2^0)^2)^{3/2}} \begin{pmatrix} -\partial_s \gamma_2^0 \\ \partial_s \gamma_1^1 \end{pmatrix} + \mathcal{O}(\varepsilon^2) & \text{otherwise.} \end{cases} \tag{28}$$

In particular, the direction of the normal vector $\boldsymbol{n}^\varepsilon_\Gamma$ depends on $\partial_s \gamma_1^0$. If $\partial_s \gamma_1^0 \neq 0$ for some $s \in [0,1]$, the interface $\Gamma^\varepsilon(t)$ is largely deformed over a region that has a width $\mathcal{O}(\varepsilon^0)$, namely, $I = [\min_{s\in[0,1]} \gamma_1^\varepsilon, \max_{s\in[0,1]} \gamma_1^\varepsilon]$ with $|I| = \mathcal{O}(\varepsilon^0)$. Therefore, there are both fluids present along a transversal segment at any $x_1 \in I$, and complicated interface dynamics occur in the limit $\varepsilon \to 0$. On the other hand, if $\partial_s \gamma_1^0 \equiv 0$, only small deformations with $|I| = \mathcal{O}(\varepsilon)$ are possible, and we obtain asymptotically a sharp transition from fluid I to fluid II at γ_1^0.

3.1 | Flow in the bulk domains

First, we consider the flow in the bulk domains Ω^ε_m, $m \in \{\text{I}, \text{II}\}$, and solve the resulting equations away from the interface. Inserting the homogenization ansatz into Equations (15–22) using (A1)–(A6) and a Taylor expansion around $x_2 = w^0(x_1)$ for Equation (22), one obtains

$$\mathcal{O}(\varepsilon) = \partial_{x_1} p^0_{\text{I}} - \partial^2_{x_2} u^0_{\text{I},1} \qquad \text{in } \Omega^\varepsilon_{\text{I}}(t), \tag{29}$$

$$\mathcal{O}(\varepsilon^0) = \varepsilon^{-1}\partial_{x_2} p_{\mathrm{I}}^0 \qquad \text{in } \Omega_{\mathrm{I}}^\varepsilon(t), \tag{30}$$

$$\mathcal{O}(\varepsilon) = \partial_{x_1} p_{\mathrm{II}}^0 - \mathrm{M}\partial_{x_2}^2 u_{\mathrm{II},1}^0 \qquad \text{in } \Omega_{\mathrm{II}}^\varepsilon(t), \tag{31}$$

$$\mathcal{O}(\varepsilon^0) = \varepsilon^{-1}\partial_{x_2} p_{\mathrm{II}}^0 \qquad \text{in } \Omega_{\mathrm{II}}^\varepsilon(t), \tag{32}$$

$$\mathcal{O}(\varepsilon) = \varepsilon^{-1}\partial_{x_2} u_{m,2}^0 + \left(\partial_{x_1} u_{m,1}^0 + \partial_{x_2} u_{m,2}^1\right) \qquad \text{in } \Omega_m^\varepsilon(t), \tag{33}$$

$$\mathcal{O}(\varepsilon^2) = u_{m,2}^0 + \varepsilon u_{m,2}^1, \qquad \mathcal{O}(\varepsilon) = \partial_{x_2} u_{m,1}^0 \qquad \text{at } x_2 = 0, \tag{34}$$

$$\mathcal{O}(\varepsilon) = \partial_{x_2} p_m^0 \qquad \text{at } x_2 = 0, \tag{35}$$

$$\mathcal{O}(\varepsilon) = p_{\mathrm{I}}^0 - p_{\mathrm{in}}^0, \qquad \mathcal{O}(\varepsilon^2) = u_{\mathrm{I},2}^0 + \varepsilon u_{\mathrm{I},2}^1 \qquad \text{or} \tag{36}$$

$$\mathcal{O}(\varepsilon^2) = \boldsymbol{u}_{\mathrm{I}}^0 - \boldsymbol{u}_{\mathrm{in}}^0 + \varepsilon\left(\boldsymbol{u}_{\mathrm{I}}^1 - \boldsymbol{u}_{\mathrm{in}}^1\right) \qquad \text{at } x_1 = 0, \tag{37}$$

$$\mathcal{O}(\varepsilon) = p_{\mathrm{II}}^0, \qquad \mathcal{O}(\varepsilon^2) = u_{\mathrm{II},2}^0 + \varepsilon u_{\mathrm{II},2}^1 \qquad \text{at } x_1 = 1, \tag{38}$$

$$\mathcal{O}(\varepsilon) = u_{m,1}^0 + \lambda^0 \partial_{x_2} u_{m,1}^0 \qquad \text{at } x_2 = w^0(x_1), \tag{39}$$

$$\mathcal{O}(\varepsilon^2) = u_{m,2}^0 + \varepsilon\left(u_{m,2}^1 + w^1 \partial_{x_2} u_{m,2}^0 - u_{m,1}^0 \partial_{x_1} w^0\right) \qquad \text{at } x_2 = w^0(x_1). \tag{40}$$

Note that either Equation (36) or Equation (37) holds, depending on the choice of the boundary condition at the inlet $\Gamma_{\mathrm{in}}^\varepsilon$.

Since we are interested in the flow behavior away from the interface $\Gamma^\epsilon(t)$, we define

$$G_{\mathrm{I}}(t) := \min_{s\in[0,1]} \gamma_1^0(s,t), \qquad G_{\mathrm{II}}(t) := \max_{s\in[0,1]} \gamma_1^0(s,t),$$

and investigate the problem for $x_1 < G_{\mathrm{I}}(t)$ in fluid I and for $x_1 > G_{\mathrm{II}}(t)$ in fluid II, respectively. In leading order, one obtains $\partial_{x_2} u_{m,2}^0 = 0$ in $\Omega_m^\varepsilon(t)$ for both $m \in \{\mathrm{I}, \mathrm{II}\}$ by the mass conservation Equation (33). The symmetry and wall boundary conditions, Equations (34,40), lead to

$$u_{m,2}^0 = 0 \text{for } m = \mathrm{I},\ x_1 < G_{\mathrm{I}}(t), \qquad \text{and for } m = \mathrm{II}, x_1 > G_{\mathrm{II}}(t),$$

which agrees with Equations (36-38), the in- and outflow boundary conditions. The second component of the momentum equation (30) of fluid I yields in leading order $\partial_{x_2} p_{\mathrm{I}}^0 = 0$ in $\Omega_{\mathrm{I}}^\varepsilon(t)$, which is in agreement with the symmetry condition, Equation (35). We conclude

$$p_{\mathrm{I}}^0 = p_{\mathrm{I}}^0(t, x_1) \qquad \text{for } x_1 < G_{\mathrm{I}}(t).$$

Analogously, the second component of the momentum equation (32) of fluid II leads to $\partial_{x_2} p_{\mathrm{II}}^0 = 0$ in $\Omega_{\mathrm{II}}^\varepsilon(t)$ (in agreement with the symmetry condition, Equation (35)), and thus

$$p_{\mathrm{II}}^0 = p_{\mathrm{II}}^0(t, x_1) \qquad \text{for } x_1 > G_{\mathrm{II}}(t).$$

From the first component of the momentum equation (29) of fluid I one obtains

$$\partial_{x_1} p_{\mathrm{I}}^0 = \partial_{x_2}^2 u_{\mathrm{I},1}^0 \qquad \text{in } \Omega_{\mathrm{I}}^{\varepsilon}(t).$$

Integrating twice over x_2 using the symmetry and wall boundary conditions, Equations (34,39), this leads to

$$u_{\mathrm{I},1}^0(t,\boldsymbol{x}) = \frac{x_2^2 - w^0(x_1)(2\lambda^0 + w^0(x_1))}{2}\partial_{x_1} p_{\mathrm{I}}^0(t,x_1) \qquad \text{for } x_1 < G_{\mathrm{I}}(t). \tag{41}$$

In a similar fashion, one obtains for fluid II by Equations (31,34,39)

$$u_{\mathrm{II},1}^0(t,\boldsymbol{x}) = \frac{x_2^2 - w^0(x_1)(2\lambda^0 + w^0(x_1))}{2\mathrm{M}}\partial_{x_1} p_{\mathrm{II}}^0(t,x_1) \qquad \text{for } x_1 > G_{\mathrm{II}}(t). \tag{42}$$

Integrating Equations (41–42) over $x_2 \in [0, w^0(x_1)]$ for any $x_1 < G_{\mathrm{I}}$ and $x_1 > G_{\mathrm{II}}$, respectively, and using Remark 2 yields

$$q(t) = \int_0^{w^0(a)} u_{\mathrm{I},1}^0(t,\boldsymbol{x})|_{x_1=a} dx_2 = -\frac{(w^0(x_1))^2(3\lambda^0 + w^0(x_1))}{3}\partial_{x_1} p_{\mathrm{I}}^0(t,x_1), \tag{43}$$

$$q(t) = \int_0^{w^0(a)} u_{\mathrm{II},1}^0(t,\boldsymbol{x})|_{x_1=a} dx_2 = -\frac{(w^0(x_1))^2(3\lambda^0 + w^0(x_1))}{3\mathrm{M}}\partial_{x_1} p_{\mathrm{II}}^0(t,x_1), \tag{44}$$

where $q(t) := \int_0^1 u_{\mathrm{I},1}^0(t,\boldsymbol{x})dx_2$. Note that q is independent of x_1, and it is equivalent to the one in (A6) if Equation (37) is given. Otherwise, q is unknown and must be found in the further solution process. Solving the above equations for p_m^0, with the outflow boundary condition, Equation (38), we obtain

$$p_{\mathrm{I}}^0(t,\boldsymbol{x}) = p_{\mathrm{in}}^0(t) - q(t)\int_0^{x_1} \frac{3}{(w^0(\xi))^2(3\lambda^0 + w^0(\xi))} d\xi \qquad \text{for } x_1 < G_{\mathrm{I}}(t), \tag{45}$$

$$p_{\mathrm{II}}^0(t,\boldsymbol{x}) = q(t)\int_{x_1}^1 \frac{3\mathrm{M}}{(w^0(\xi))^2(3\lambda^0 + w^0(\xi))} d\xi \qquad \text{for } x_1 > G_{\mathrm{II}}(t). \tag{46}$$

Here, the inlet pressure $p_{\mathrm{in}}^0(t)$ is either given by the inlet boundary condition, Equation (36), or has to be found in the further solution process. Note that since the inlet boundary condition is either Equation (36) or Equation (37), this means that either q or p_{in}^0 is given, while the other still must be determined. Inserting Equations (45–46) into Equations (41–42) yields

$$u_{\mathrm{I},1}^0(t,\boldsymbol{x}) = 3q(t)\frac{w^0(x_1)(2\lambda^0 + w^0(x_1)) - x_2^2}{2(w^0(x_1))^2(3\lambda^0 + w^0(x_1))} \qquad \text{for } x_1 < G_{\mathrm{I}}(t), \tag{47}$$

$$u^0_{\mathrm{II},1}(t,\boldsymbol{x}) = 3q(t)\frac{w^0(x_1)(2\lambda^0 + w^0(x_1)) - x_2^2}{2(w^0(x_1))^2(3\lambda^0 + w^0(x_1))} \qquad \text{for } x_1 > G_{\mathrm{II}}(t). \tag{48}$$

Using Equations (47–48) in the mass conservation Equation (33), the first-order equations become

$$\partial_{x_2} u^1_{m,2} = q(t)\left(\frac{1}{2(3\lambda^0+w^0(x_1))^2} + \frac{1}{(w^0(x_1))^2} - \frac{9(2\lambda^0+w^0(x_1))x_2^2}{2(w^0(x_1))^3(3\lambda^0+w^0(x_1))^2}\right)\partial_{x_1} w^0(x_1),$$

for $m \in \{\mathrm{I}, \mathrm{II}\}$. Integration over x_2 using the symmetry condition, Equation (34), yields

$$u^1_{\mathrm{I},2}(t,\boldsymbol{x}) = q(t)\left(\frac{x_2}{2(3\lambda^0 + w^0(x_1))^2} + \frac{x_2}{(w^0(x_1))^2} - \frac{3(2\lambda^0 + w^0(x_1))x_2^3}{2(w^0(x_1))^3(3\lambda^0 + w^0(x_1))^2}\right)\partial_{x_1} w^0(x_1) \quad \text{for } x_1 < G_{\mathrm{I}}(t),$$

$$u^1_{\mathrm{II},2}(t,\boldsymbol{x}) = q(t)\left(\frac{x_2}{2(3\lambda^0 + w^0(x_1))^2} + \frac{x_2}{(w^0(x_1))^2} - \frac{3(2\lambda^0 + w^0(x_1))x_2^3}{2(w^0(x_1))^3(3\lambda^0 + w^0(x_1))^2}\right)\partial_{x_1} w^0(x_1) \qquad \text{for } x_1 > G_{\mathrm{II}}(t),$$

which is in agreement with the boundary conditions, Equations (36-38,40).

Summarizing, we obtain the following solution in the bulk domains. There holds

$$\boldsymbol{u}^\varepsilon_{\mathrm{I}}(t,\boldsymbol{x}) = q(t)\begin{pmatrix} 3\frac{w^0(x_1)(2\lambda^0+w^0(x_1))-x_2^2}{2(w^0(x_1))^2(3\lambda^0+w^0(x_1))} + \mathcal{O}(\varepsilon) \\ \varepsilon\left(\frac{x_2}{2(3\lambda^0+w^0(x_1))^2} + \frac{x_2}{(w^0(x_1))^2} - \frac{3(2\lambda^0+w^0(x_1))x_2^3}{2(w^0(x_1))^3(3\lambda^0+w^0(x_1))^2}\right)\partial_{x_1} w^0(x_1) + \mathcal{O}(\varepsilon^2) \end{pmatrix}, \tag{49}$$

$$p^\varepsilon_{\mathrm{I}}(t,\boldsymbol{x}) = p^0_{\mathrm{in}}(t) - q(t)\int_0^{x_1} \frac{3}{(w^0(\xi))^2(3\lambda^0 + w^0(\xi))}d\xi + \mathcal{O}(\varepsilon) \tag{50}$$

for $x_1 < G_{\mathrm{I}}(t)$, while for $x_1 > G_{\mathrm{II}}(t)$ one gets

$$\boldsymbol{u}^\varepsilon_{\mathrm{II}}(t,\boldsymbol{x}) = q(t)\begin{pmatrix} 3\frac{w^0(x_1)(2\lambda^0+w^0(x_1))-x_2^2}{2(w^0(x_1))^2(3\lambda^0+w^0(x_1))} + \mathcal{O}(\varepsilon) \\ \varepsilon\left(\frac{x_2}{2(3\lambda^0+w^0(x_1))^2} + \frac{x_2}{(w^0(x_1))^2} - \frac{3(2\lambda^0+w^0(x_1))x_2^3}{2(w^0(x_1))^3(3\lambda^0+w^0(x_1))^2}\right)\partial_{x_1} w^0(x_1) + \mathcal{O}(\varepsilon^2) \end{pmatrix}, \tag{51}$$

$$p^\varepsilon_{\mathrm{II}}(t,\boldsymbol{x}) = q(t)\int_{x_1}^1 \frac{3\mathrm{M}}{(w^0(\xi))^2(3\lambda^0 + w^0(\xi))}d\xi + \mathcal{O}(\varepsilon). \tag{52}$$

This means that the solution in the bulk domains is of Hagen–Poiseuille type. Depending on the chosen inlet boundary condition, Equation (36) or Equation (37), either the inlet pressure p^0_{in} or the total flux q is given. The other coefficient will be determined in the following subsection via

the coupling at the interface $\Gamma^\epsilon(t)$. For upscaled models, we emphasize that the total flux q is independent of the position x_1 and that the pressures p_m^0, $m \in \{\mathrm{I}, \mathrm{II}\}$, depend linearly on q with a coefficient that only depends on the geometry (w^0), the viscosity ratio M, and the slip length λ^0.

3.2 | Interface with small deformations

We continue the analysis for the interface region around $\Gamma^\epsilon(t)$. We first show that the bulk solutions are not compatible with the interface conditions Equations (23–26). However, introduction of a suitable scaling allows to find the asymptotic solution in the boundary layer around the interface $\Gamma^\epsilon(t)$, which connects the bulk domain solutions. In addition to (A1)–(A6), we make the following assumptions:

(A7) The leading order interface position in x_1 is constant, that is, $\partial_s \gamma_1^0 \equiv 0$.
(A8) The capillary number is given by $\mathrm{Ca} = \varepsilon^\alpha \overline{\mathrm{Ca}}$ for some $\alpha \in \mathbb{N}_0$. Here, $\overline{\mathrm{Ca}}$ denotes the effective capillary number and is independent of ε.

Note that (A7) means that the fluid–fluid interface Γ^ϵ has only small deformations, such that $G_\mathrm{I}(t) = \gamma_1^0(t) = G_\mathrm{II}(t)$. Furthermore, (A8) is used to distinguish whether interfacial tension is relevant or even dominating the interface movement (see also Remark 3). In the alternative case of a largely deformed interface ($\partial_s \gamma_1^0 \not\equiv 0$), both fluids are present along a transversal segment since the interface is partly horizontal (cf. Equation (28)). This leads to complicated interface dynamics and requires a detailed analysis of further boundary layers due to the symmetry and boundary conditions Equations (25– 26), which yield $\partial_s \gamma_1^0(t, s) = 0$ for $s \in \{0, 1\}$. However, this lies outside the scope of this paper.

Inserting the homogenization ansatz into the kinematic interface condition, Equation (23), gives

$$(\partial_t \gamma_1^0 - u_{\mathrm{I},1}^0)\partial_s \gamma_2^0 + u_{\mathrm{I},2}^0 \partial_s \gamma_1^1 = \mathcal{O}(\varepsilon).$$

Since γ_1^0 is constant in the parameter s, a nonsingular parameterization requires $\partial_s \gamma_2^0 > 0$. Inserting the bulk solution Equation (49), where $u_{\mathrm{I},2}^0 = 0$, yields in leading order

$$\partial_t \gamma_1^0 = 3q \frac{w^0(\gamma_1^0)(2\lambda^0 + w^0(\gamma_1^0)) - (\gamma_2^0)^2}{2(w^0(\gamma_1^0))^2(3\lambda^0 + w^0(\gamma_1^0))},$$

which contradicts the assumption that γ_1^0 does not depend on s, except for the trivial case $q(t) = 0$. Therefore, we expect the existence of a boundary layer around the interface $\Gamma^\epsilon(t)$. Here, the idea of the matched asymptotic expansion method is to find an asymptotic solution of the problem in rescaled, so-called inner coordinates close to the interface (the boundary layer). This solution must satisfy the interface conditions and match the previously derived, so-called outer solution in the bulk regions given by Equations (49–52). The combination of inner and outer solutions then solves the problem in the whole domain. For a detailed introduction to matched asymptotic expansion method, we refer to Ref. 75.

To resolve the boundary layer, we apply the inner scaling

$$X_1(t,x_1) := (x_1 - \gamma_1^0(t))/\varepsilon, \qquad X_2 := x_2$$

and use the rescaled variables and domains (see also Table 1)

$$\boldsymbol{Y}^\varepsilon := \begin{pmatrix} (\gamma_1^\varepsilon - \gamma_1^0)/\varepsilon \\ \gamma_2^\varepsilon \end{pmatrix}, \quad U_m^\varepsilon(t,\boldsymbol{X}) := \boldsymbol{u}_m^\varepsilon(t,\boldsymbol{x}), \quad P_m^\varepsilon(t,\boldsymbol{X}) := p_m^\varepsilon(t,\boldsymbol{x}),$$

$$\Omega_{\boldsymbol{X}}^\varepsilon(t) := \{\boldsymbol{X} \in \mathbb{R}^2 \mid 0 < X_2 < w^\varepsilon(\gamma_1^0(t) + \varepsilon X_1)\}, \quad \Gamma_{\boldsymbol{X}}^\varepsilon(t) := \{\boldsymbol{Y}^\varepsilon(t,s) \mid s \in [0,1]\},$$

$$\Omega_{\boldsymbol{X},\mathrm{I}}^\varepsilon(t) := \{\boldsymbol{X}(t,\boldsymbol{x}) \mid \boldsymbol{x} \in \Omega_{\mathrm{I}}^\varepsilon\}, \quad \Omega_{\boldsymbol{X},\mathrm{II}}^\varepsilon(t) := \{\boldsymbol{X}(t,\boldsymbol{x}) \mid \boldsymbol{x} \in \Omega_{\mathrm{II}}^\varepsilon\},$$

$$\Gamma_{\boldsymbol{X},\mathrm{w},m}^\varepsilon(t) := \{\boldsymbol{X} \in \partial\Omega_{\boldsymbol{X},m}^\varepsilon(t) \mid X_2 = w^\varepsilon(\gamma_1^0(t) + \varepsilon X_1)\}.$$

The matching conditions between inner expansion in terms of $\boldsymbol{X}$ and outer expansion in terms of $\boldsymbol{x}$ require the equivalence in the limit, that is, for any outer quantity $a_m^\varepsilon(t,\boldsymbol{x})$ with inner expansion $A_m^\varepsilon(t,\boldsymbol{X})$ there must hold $\lim_{x_1 \to \gamma_1^0} a_m^\varepsilon(t,\boldsymbol{x}) = \lim_{X_1 \to (-1)^m \infty} A_m^\varepsilon(t,\boldsymbol{X})|_{X_2=x_2}$. With the rescaled coordinates, Equations (15-19) and Equations (22–26) become

$$\varepsilon^2 \mathrm{Re}\left(\varepsilon\partial_t U_{\mathrm{I}}^\varepsilon - \partial_{X_1} U_{\mathrm{I}}^\varepsilon \partial_t \gamma_1^0 + (U_{\mathrm{I}}^\varepsilon \cdot \nabla_{\boldsymbol{X}}) U_{\mathrm{I}}^\varepsilon\right) + \nabla_{\boldsymbol{X}} P_{\mathrm{I}}^\varepsilon = \varepsilon \Delta_{\boldsymbol{X}} U_{\mathrm{I}}^\varepsilon \qquad \text{in } \Omega_{\boldsymbol{X},\mathrm{I}}^\varepsilon(t), \tag{53}$$

$$\varepsilon^2 \mathrm{R}\mathrm{Re}\left(\varepsilon\partial_t U_{\mathrm{II}}^\varepsilon - \partial_{X_1} U_{\mathrm{II}}^\varepsilon \partial_t \gamma_1^0 + (U_{\mathrm{II}}^\varepsilon \cdot \nabla_{\boldsymbol{X}}) U_{\mathrm{II}}^\varepsilon\right) + \nabla_{\boldsymbol{X}} P_{\mathrm{II}}^\varepsilon = \mathrm{M}\varepsilon \Delta_{\boldsymbol{X}} U_{\mathrm{II}}^\varepsilon \qquad \text{in } \Omega_{\boldsymbol{X},\mathrm{II}}^\varepsilon(t), \tag{54}$$

$$\nabla_{\boldsymbol{X}} \cdot U_m^\varepsilon = 0 \qquad \text{in } \Omega_{\boldsymbol{X},m}^\varepsilon(t), \tag{55}$$

$$U_m^\varepsilon \cdot \boldsymbol{n}_{\mathrm{sym}} = 0, \quad \boldsymbol{t}_{\mathrm{sym}} \cdot \nabla_{\boldsymbol{X}} U_m^\varepsilon \boldsymbol{n}_{\mathrm{sym}} = 0 \qquad \text{at } X_2 = 0, \tag{56}$$

$$\nabla_{\boldsymbol{X}} P_m^\varepsilon \cdot \boldsymbol{n}_{\mathrm{sym}} = 0, \qquad \text{at } X_2 = 0, \tag{57}$$

$$\boldsymbol{T}_{\mathrm{w}}^\varepsilon \cdot (U_m^\varepsilon + 2\lambda^\varepsilon \mathbf{D}_{\boldsymbol{X}}(U_m^\varepsilon)\boldsymbol{N}_{\mathrm{w}}^\varepsilon) = 0, \quad U_m^\varepsilon \cdot \boldsymbol{N}_{\mathrm{w}}^\varepsilon = 0 \qquad \text{on } \Gamma_{\boldsymbol{X},\mathrm{w},m}^\varepsilon(t), \tag{58}$$

$$\partial_t \gamma_1^0 N_{\Gamma,1}^\varepsilon + \varepsilon \partial_t \boldsymbol{Y}^\varepsilon \cdot \boldsymbol{N}_\Gamma^\varepsilon = U_{\mathrm{I}}^\varepsilon \cdot \boldsymbol{N}_\Gamma^\varepsilon, \quad U_{\mathrm{I}}^\varepsilon = U_{\mathrm{II}}^\varepsilon \qquad \text{on } \Gamma_{\boldsymbol{X}}^\varepsilon(t), \tag{59}$$

$$-(P_{\mathrm{I}}^\varepsilon - P_{\mathrm{II}}^\varepsilon)\boldsymbol{N}_\Gamma^\varepsilon + 2\varepsilon\left(\mathbf{D}_{\boldsymbol{X}}(U_{\mathrm{I}}^\varepsilon) - \mathrm{M}\mathbf{D}_{\boldsymbol{X}}(U_{\mathrm{II}}^\varepsilon)\right)\boldsymbol{N}_\Gamma^\varepsilon = \frac{\varepsilon^2}{\mathrm{Ca}} K^\varepsilon \boldsymbol{N}_\Gamma^\varepsilon \qquad \text{on } \Gamma_{\boldsymbol{X}}^\varepsilon(t), \tag{60}$$

$$\boldsymbol{N}_\Gamma^\varepsilon \cdot \boldsymbol{n}_{\mathrm{sym}} = 0 \qquad \text{at } s = 0, \tag{61}$$

$$\cos\left(\theta^\varepsilon\left(-\partial_t(\gamma_1^0 T_{\mathrm{w},1}^\varepsilon + \varepsilon \boldsymbol{Y}^\varepsilon \cdot \boldsymbol{T}_{\mathrm{w}}^\varepsilon)|_{X_1 = Y_1^\varepsilon}\right)\right) = \boldsymbol{T}_\Gamma^\varepsilon \cdot \boldsymbol{T}_{\mathrm{w}}^\varepsilon|_{X_1 = Y_1^\varepsilon} \qquad \text{at } s = 1. \tag{62}$$

The transformed normal and tangential vectors are given by

$$\boldsymbol{T}_{\mathrm{w}}^\varepsilon = \boldsymbol{t}_{\mathrm{w}}^\varepsilon|_{x_1 = \gamma_1^0 + \varepsilon X_1}, \boldsymbol{N}_{\mathrm{w}}^\varepsilon = \boldsymbol{n}_{\mathrm{w}}^\varepsilon|_{x_1 = \gamma_1^0 + \varepsilon X_1},$$

$$\boldsymbol{T}_\Gamma^\varepsilon = \frac{1}{\sqrt{(\partial_s Y_1^\varepsilon)^2 + (\partial_s Y_2^\varepsilon)^2}} \partial_s \boldsymbol{Y}^\varepsilon, \boldsymbol{N}_\Gamma^\varepsilon = \frac{1}{\sqrt{(\partial_s Y_1^\varepsilon)^2 + (\partial_s Y_2^\varepsilon)^2}} \begin{pmatrix} \partial_s Y_2^\varepsilon \\ -\partial_s Y_1^\varepsilon \end{pmatrix},$$

and the rescaled curvature K^ε is

$$K^\varepsilon = \frac{\partial_s Y_1^\varepsilon \partial_s^2 Y_2^\varepsilon - \partial_s Y_2^\varepsilon \partial_s^2 Y_1^\varepsilon}{\varepsilon\left((\partial_s Y_1^\varepsilon)^2 + (\partial_s Y_2^\varepsilon)^2\right)^{3/2}}.$$

Inserting the homogenization ansatz into Equations (53–62) using (A1)–(A5), (A7), (A8), and a Taylor expansion around $X_2 = w^0(\gamma_1^0(t))$ for Equation (58), one obtains

$$\mathcal{O}(\varepsilon^2) = \nabla_{\boldsymbol{X}} P_{\mathrm{I}}^0 + \varepsilon\left(\nabla_{\boldsymbol{X}} P_{\mathrm{I}}^1 - \Delta_{\boldsymbol{X}} \boldsymbol{U}_{\mathrm{I}}^0\right) \quad \text{in } \Omega_{\boldsymbol{X},\mathrm{I}}^\varepsilon(t), \tag{63}$$

$$\mathcal{O}(\varepsilon^2) = \nabla_{\boldsymbol{X}} P_{\mathrm{II}}^0 + \varepsilon\left(\nabla_{\boldsymbol{X}} P_{\mathrm{II}}^1 - \mathrm{M}\Delta_{\boldsymbol{X}} \boldsymbol{U}_{\mathrm{II}}^0\right) \quad \text{in } \Omega_{\boldsymbol{X},\mathrm{II}}^\varepsilon(t), \tag{64}$$

$$\mathcal{O}(\varepsilon) = \nabla_{\boldsymbol{X}} \cdot \boldsymbol{U}_m^0 \quad \text{in } \Omega_{\boldsymbol{X},m}^\varepsilon(t), \tag{65}$$

$$\mathcal{O}(\varepsilon) = U_{m,2}^0, \qquad \mathcal{O}(\varepsilon) = \partial_{X_2} U_{m,1}^0 \quad \text{at } X_2 = 0, \tag{66}$$

$$\mathcal{O}(\varepsilon^2) = \partial_{X_2} P_m^0 + \varepsilon \partial_{X_2} P_m^1 \quad \text{at } X_2 = 0, \tag{67}$$

$$\mathcal{O}(\varepsilon) = U_{m,1}^0 + \left(\lambda^0 + \lambda_e \exp(-|X_1|)\right)\left(\partial_{X_2} U_{m,1}^0 + \partial_{X_1} U_{m,2}^0\right) \quad \text{at } X_2 = w^0(\gamma_1^0(t)), \tag{68}$$

$$\mathcal{O}(\varepsilon) = U_{m,2}^0 \quad \text{at } X_2 = w^0(\gamma_1^0(t)), \tag{69}$$

$$\mathcal{O}(\varepsilon) = \left(\partial_t \gamma_1^0 - U_{\mathrm{I},1}^0\right)\partial_s Y_2^0 + U_{\mathrm{I},2}^0 \partial_s Y_1^0 \quad \text{on } \Gamma_{\boldsymbol{X}}^\varepsilon(t), \tag{70}$$

$$\mathcal{O}(\varepsilon) = \boldsymbol{U}_{\mathrm{I}}^0 - \boldsymbol{U}_{\mathrm{II}}^0 \quad \text{on } \Gamma_{\boldsymbol{X}}^\varepsilon(t), \tag{71}$$

$$\mathcal{O}(\varepsilon^{\min(1,2-\alpha)}) = (P_{\mathrm{I}}^0 - P_{\mathrm{II}}^0) + \frac{\varepsilon^{1-\alpha}}{\overline{\mathrm{Ca}}} \frac{\partial_s Y_1^0 \partial_s^2 Y_2^0 - \partial_s Y_2^0 \partial_s^2 Y_1^0}{\left((\partial_s Y_1^0)^2 + (\partial_s Y_2^0)^2\right)^{3/2}} \quad \text{on } \Gamma_{\boldsymbol{X}}^\varepsilon(t), \tag{72}$$

$$\mathcal{O}(\varepsilon) = \partial_s \boldsymbol{Y}^0 \cdot \left(\mathbf{D}_{\boldsymbol{X}}(\boldsymbol{U}_{\mathrm{I}}^0) - \mathrm{M}\mathbf{D}_{\boldsymbol{X}}(\boldsymbol{U}_{\mathrm{II}}^0)\right)\begin{pmatrix} \partial_s Y_2^0 \\ -\partial_s Y_1^0 \end{pmatrix} \quad \text{on } \Gamma_{\boldsymbol{X}}^\varepsilon(t), \tag{73}$$

$$\mathcal{O}(\varepsilon) = \partial_s Y_1^0 \quad \text{at } s = 0, \tag{74}$$

$$\mathcal{O}(\varepsilon) = \frac{\partial_s Y_1^0}{\sqrt{(\partial_s Y_1^0)^2 + (\partial_s Y_2^0)^2}} + \cos(\theta^0(\partial_t \gamma_1^0)) \quad \text{at } s = 1. \tag{75}$$

The leading order terms in the momentum equations (63–64) yield $\nabla_{\boldsymbol{X}} P_m^0 = \mathbf{0}$ in $\Omega_{\boldsymbol{X},m}^\varepsilon(t)$ for $m \in \{\mathrm{I}, \mathrm{II}\}$. This is in agreement with the symmetry condition, Equation (67). By matching with

the outer solution we obtain

$$P_m^0(t,\boldsymbol{X}) = p_m^0(t,\gamma_1^0(t)) \qquad \text{for all } \boldsymbol{X} \in \Omega_{\boldsymbol{X},m}^{\varepsilon}(t). \tag{76}$$

Remark 3. Recall that we assume $\mathrm{Ca} = \varepsilon^{\alpha}\overline{\mathrm{Ca}}$ for some $\alpha \in \mathbb{N}_0$. Considering Equation (72), one must distinguish the cases $\alpha < 1$, $\alpha = 1$, and $\alpha > 1$. For $\alpha < 1$, the interface tension force is negligible in leading order, such that the pressures P_{I}^0 and P_{II}^0 are equal. Formally, this allows to determine the leading order solution of the outer bulk-flow problem. However, this also means that the interface $\Gamma_{\boldsymbol{X}}^{\varepsilon}(t)$ is not stabilized by surface tension, but part of the first-order solution, such that we cannot guarantee solvability. Furthermore, one might expect the occurrence of topological changes due to, for example, formation of bubbles, thin films, and so forth, which are not part of this model. In the case $\alpha > 1$, the interfacial tension force is dominating Equation (72), so that the leading order curvature K^0 of the interface is zero. Due to the boundary conditions, Equations (74–75), this can only happen if the leading order contact angle $\theta^0(\partial_t\gamma_1^0)$ is $\pi/2$ for any $\gamma_1^0(t)$, that is, for a constant contact angle model for perfectly mixed-wet materials. Even worse, due to Equation (76), the leading order solution of the outer bulk-flow problem then depends on the first-order solution, such that we cannot assure the solvability in this case either. We therefore consider in what follows only the case $\alpha = 1$. Then the pressure difference is balanced by the surface tension force in Equation (72). This leads to a solution for the outer bulk-flow problem as well as for the interface shape.

In the regime $\alpha = 1$, plugging the constant pressures from Equation (76) into the interfacial force balance equation (72) yields a constant leading-order curvature K^0 given by

$$K^0 = \frac{\partial_s Y_2^0 \partial_s^2 Y_1^0 - \partial_s Y_1^0 \partial_s^2 Y_2^0}{\left((\partial_s Y_1^0)^2 + (\partial_s Y_2^0)^2\right)^{3/2}} = \overline{\mathrm{Ca}}(p_{\mathrm{II}}^0 - p_{\mathrm{I}}^0)|_{x_1=\gamma_1^0}. \tag{77}$$

Therefore, the interface is a circular arc. By the contact-angle equation (75), one obtains

$$K^0 = -\frac{\cos(\theta^0(\partial_t\gamma_1^0))}{w^0(\gamma_1^0)}. \tag{78}$$

Combining Equations (77) and (78) and plugging the result into the bulk pressure solutions given in Equations (50, 52) leads to

$$p_{\mathrm{in}}^0 - q\left(\int_0^{\gamma_1^0} \frac{3}{(w^0(x_1))^2(3\lambda^0 + w^0(x_1))}dx_1 + \int_{\gamma_1^0}^1 \frac{3\mathrm{M}}{(w^0(x_1))^2(3\lambda^0 + w^0(x_1))}dx_1\right) = \frac{\cos(\theta^0(\partial_t\gamma_1^0))}{\overline{\mathrm{Ca}}w^0(\gamma_1^0)}. \tag{79}$$

Due to the constant curvature in Equation (78) and the symmetry condition, Equation (74), the leading order interface $\Gamma^0_{\boldsymbol{X}}(t) := \{\boldsymbol{Y}^0(t,s) \mid s \in [0,1]\}$ is given (up to a reparameterization) by

$$\boldsymbol{Y}^0(t,s) = \begin{cases} \frac{w^0(\gamma_1^0)}{\cos(\theta^0(\partial_t\gamma_1^0))} \begin{pmatrix} \cos\left((\frac{\pi}{2} - \theta^0(\partial_t\gamma_1^0))s\right) - \sin\left(\theta^0(\partial_t\gamma_1^0)\right) \\ \sin\left((\frac{\pi}{2} - \theta^0(\partial_t\gamma_1^0))s\right) \end{pmatrix} & \text{for } \theta^0 \neq \pi/2, \\ w^0(\gamma_1^0(t)) \begin{pmatrix} 0 \\ s \end{pmatrix} & \text{for } \theta^0 = \pi/2. \end{cases}$$

Analogously to Remark 2, by the mass conservation Equation (17), the interface velocity Equation (59), and the outer velocity solution given in Equation (49), we obtain

$$\begin{aligned} 0 &= \int_{\Omega_{\mathrm{I}}^\varepsilon} \nabla^\varepsilon \cdot \boldsymbol{u}_{\mathrm{I}}^\varepsilon d\boldsymbol{x} = \int_{\Gamma^\varepsilon} \boldsymbol{u}_{\mathrm{I}}^\varepsilon \cdot \boldsymbol{n}_\Gamma^\varepsilon dl - \int_0^1 u_{\mathrm{I},1}^\varepsilon|_{x_1=0} dx_1 \\ &= \int_{\Gamma^\varepsilon} \partial_t\gamma_1^0 N_{\Gamma,1}^\varepsilon + \varepsilon\partial_t \boldsymbol{Y}^\varepsilon \cdot \boldsymbol{N}_\Gamma^\varepsilon dl - q + \mathcal{O}(\varepsilon) = \int_0^1 \partial_t\gamma_1^0 \partial_s Y_{\mathrm{w}2}^\varepsilon ds - q + \mathcal{O}(\varepsilon) \\ &= \partial_t\gamma_1^0 w^0(\gamma_1^0) - q + \mathcal{O}(\varepsilon). \end{aligned}$$

Therefore, the leading order position γ_1^0 of the interface fulfils

$$\partial_t\gamma_1^0(t) = \frac{q(t)}{w^0(\gamma_1^0(t))}. \tag{80}$$

To find the solution for $\boldsymbol{u}_m^0$, p_m^0 ($m \in \{\mathrm{I}, \mathrm{II}\}$), which is given by Equations (49–52), one has to determine γ_1^0, q, and p_{in}^0. The derivation depends on the chosen inlet boundary condition. For a given inlet velocity $\boldsymbol{u}_{\mathrm{I}}^\varepsilon = \boldsymbol{u}_{\mathrm{in}}^\varepsilon$ at $\Gamma_{\mathrm{in}}^\varepsilon$, the value of q is known. Plugging q into Equation (80) and solving for γ_1^0 yields

$$\gamma_1^0(t) = \mathcal{W}^{-1}\left(\mathcal{W}(\gamma_1^0|_{t=0}) + \int_0^t q(\tau)d\tau\right),$$

where $\mathcal{W}(\xi) := \int_0^\xi w^0(x_1)dx_1$. Note that $\mathcal{W}' = w^0 > 0$ by (A4), such that the inverse function $\mathcal{W}^{-1}$ is well-defined. Finally, p_{in}^0 can be found by Equation (79).

For a given inlet pressure $p_{\mathrm{I}}^\varepsilon = p_{\mathrm{in}}^\varepsilon$ at $\Gamma_{\mathrm{in}}^\varepsilon$, the value of p_{in}^0 is known. Then, the differential algebraic system of Equations (79–80) has index 1 and can be solved for q and γ_1^0. Inserting Equation (80) into Equation (79) and applying the implicit function theorem to find q depending on γ_1^0, a sufficient condition for solvability is

$$\sin\left(\theta^0\left(\frac{q}{w^0(\gamma_1^0)}\right)\right)(\theta^0)'\left(\frac{q}{w^0(\gamma_1^0)}\right) \neq \overline{\mathrm{Ca}}(w^0(\gamma_1^0))^2\left(\int_0^{\gamma_1^0} \frac{3}{(w^0(x_1))^2(3\lambda^0 + w^0(x_1))}dx_1 + \int_{\gamma_1^0}^1 \frac{3\mathrm{M}}{(w^0(x_1))^2(3\lambda^0 + w^0(x_1))}dx_1\right),$$

where $(\theta^0)'$ denotes the derivative of θ^0. Note that the right-hand side is always positive, so that any contact angle model which fulfils $(\theta^0)' \leq 0$ yields solvable differential algebraic equations.

Furthermore, from Equations (63-71,73), the velocity close to the interface is given by two coupled Stokes problems. More precisely, these problems are defined in the domains

$$\Omega^0_{\boldsymbol{X},\mathrm{I}}(t) = \{\boldsymbol{X} \in \mathbb{R} \times (0, w^0(\gamma_1^0(t))) \mid \exists s \in [0,1] : X_1 < Y_1^0(t,s) \wedge X_2 = Y_2^0(t,s)\},$$

$$\Omega^0_{\boldsymbol{X},\mathrm{II}}(t) = \{\boldsymbol{X} \in \mathbb{R} \times (0, w^0(\gamma_1^0(t))) \mid \exists s \in [0,1] : X_1 > Y_1^0(t,s) \wedge X_2 = Y_2^0(t,s)\}.$$

With this, the two problems are ($m \in \{\mathrm{I}, \mathrm{II}\}$)

$$0 = \nabla_{\boldsymbol{X}} P^1_{\mathrm{I}} - \Delta_{\boldsymbol{X}} \boldsymbol{U}^0_{\mathrm{I}} \quad \text{in } \Omega^0_{\boldsymbol{X},\mathrm{I}}(t), \tag{81}$$

$$0 = \nabla_{\boldsymbol{X}} P^1_{\mathrm{II}} - \mathrm{M}\Delta_{\boldsymbol{X}} \boldsymbol{U}^0_{\mathrm{II}} \quad \text{in } \Omega^0_{\boldsymbol{X},\mathrm{II}}(t), \tag{82}$$

$$0 = \nabla_{\boldsymbol{X}} \cdot \boldsymbol{U}^0_m \quad \text{in } \Omega^0_{\boldsymbol{X},m}(t), \tag{83}$$

$$0 = U^0_{m,2}, \qquad 0 = \partial_{X_2} U^0_{m,1}, \qquad 0 = \partial_{X_2} P^1_m \quad \text{at } X_2 = 0, \tag{84}$$

$$0 = U^0_{m,1} + \left(\lambda^0 + \lambda_e \exp(-|X_1|)\right)\partial_{X_2} U^0_{m,1}, \quad 0 = U^0_{m,2} \quad \text{at } X_2 = w^0(\gamma_1^0(t)), \tag{85}$$

$$0 = \left(\partial_t \gamma_1^0 - U^0_{\mathrm{I},1}\right)\partial_s Y^0_2 + U^0_{\mathrm{I},2}\partial_s Y^0_1 \quad \text{on } \Gamma^0_{\boldsymbol{X}}(t), \tag{86}$$

$$0 = \boldsymbol{U}^0_{\mathrm{I}} - \boldsymbol{U}^0_{\mathrm{II}} \quad \text{on } \Gamma^0_{\boldsymbol{X}}(t), \tag{87}$$

$$0 = \partial_s \boldsymbol{Y}^0 \cdot \left(\mathbf{D}_{\boldsymbol{X}}(\boldsymbol{U}^0_{\mathrm{I}}) - \mathrm{M}\mathbf{D}_{\boldsymbol{X}}(\boldsymbol{U}^0_{\mathrm{II}})\right)\begin{pmatrix} \partial_s Y^0_2 \\ -\partial_s Y^0_1 \end{pmatrix} \quad \text{on } \Gamma^0_{\boldsymbol{X}}(t), \tag{88}$$

$$\mathbf{0} = \lim_{X_1 \to -\infty} \boldsymbol{U}^0_{\mathrm{I}} - \boldsymbol{u}^0_{\mathrm{I}}|_{x_1 = \gamma_1^0, x_2 = X_2}, \tag{89}$$

$$\mathbf{0} = \lim_{X_1 \to \infty} \boldsymbol{U}^0_{\mathrm{II}} - \boldsymbol{u}^0_{\mathrm{II}}|_{x_1 = \gamma_1^0, x_2 = X_2}. \tag{90}$$

3.3 | Unsaturated flow limit

In (A2), we assumed the viscosity ratio $\mathrm{M} = \mathcal{O}(\varepsilon^0)$. Here, we investigate the case when the viscosity of fluid II is much smaller than that of fluid I, like in a system consisting of water and air. Hence, we replace (A2) by:

(A9) The viscosity ratio satisfies $M = \mathcal{O}(\varepsilon^\beta)$ for some $\beta \geq 1$.

Following the same steps as in the previous subsections, we obtain a model which only includes the flow of fluid I, while the flow of fluid II can be omitted. In other words, the upscaled model is an unsaturated flow in the thin strip. Furthermore, the effective solution for fluid I will coincide with the one obtained when letting $M \to 0$ in Equations (49, 50, 79, 80) derived previously.

To this end, we use the same asymptotic expansions and (A1), (A3)–(A8), and (A9) instead of (A2). For fluid I, we obtain again Equations (29,30,33-35,39,40) and work with either Equation

(36) or Equation (37) as inlet condition. Therefore, the solution for fluid I is again given by Equations (49, 50), where p^0_{in} and q are given by the interface region and the inlet condition.

For fluid II, the leading order mass balance equations become

$$\mathcal{O}(\varepsilon) = \partial_{x_1} p^0_{\text{II}} \qquad \text{in } \Omega^\varepsilon_{\text{II}}(t), \tag{91}$$

$$\mathcal{O}(\varepsilon^0) = \varepsilon^{-1}\partial_{x_2} p^0_{\text{II}} \qquad \text{in } \Omega^\varepsilon_{\text{II}}(t). \tag{92}$$

Together with the leading order outflow condition $\mathcal{O}(\varepsilon) = p^0_{\text{II}}$ at $x_1 = 1$, we conclude that $p^0_{\text{II}}(t, \boldsymbol{x}) = 0$ in $\Omega^\varepsilon_{\text{II}}(t)$. Rescaling the interface region as in Subsection 3.2 and taking (A7) and (A8) into account, the leading order equations for fluid I are again Equations (63,65-69). Since $p^0_{\text{II}} \equiv 0$, the interface conditions are Equations (68-70,74), as well as

$$\mathcal{O}(\varepsilon^{\min(1,2-\alpha)}) = P^0_{\text{I}} + \frac{\varepsilon^{1-\alpha}}{\overline{\text{Ca}}} \frac{\partial_s Y^0_1 \partial_s^2 Y^0_2 - \partial_s Y^0_2 \partial_s^2 Y^0_1}{\left((\partial_s Y^0_1)^2 + (\partial_s Y^0_2)^2\right)^{3/2}} \qquad \text{on } \Gamma^\varepsilon_{\boldsymbol{X}}(t), \tag{93}$$

$$\mathcal{O}(\varepsilon) = \partial_s \boldsymbol{Y}^0 \cdot \mathbf{D}_{\boldsymbol{X}}(\boldsymbol{U}^0_{\text{I}}) \begin{pmatrix} \partial_s Y^0_2 \\ -\partial_s Y^0_1 \end{pmatrix} \qquad \text{on } \Gamma^\varepsilon_{\boldsymbol{X}}(t). \tag{94}$$

In the regime $\alpha = 1$, this yields a constant leading-order curvature, implying

$$p^0_{\text{in}} - q \int_0^{\gamma^0_1} \frac{3}{(w^0(x_1))^2(3\lambda^0 + w^0(x_1))} dx_1 = \frac{\cos(\theta^0(\partial_t \gamma^0_1))}{\overline{\text{Ca}} w^0(\gamma^0_1)}, \tag{95}$$

$$\partial_t \gamma^0_1(t) = \frac{q(t)}{w^0(\gamma^0_1(t))}. \tag{96}$$

3.4 | Hysteretic contact angle model

The previous analysis requires that the dynamic contact angle relation is continuous, as expressed in (A5). However, experiments suggest the occurrence of contact angle hysteresis. For example, the reviews[68,70] discuss this as a result of surface wettability and roughness. This means that static contact angles are not unique, but can vary due to pinning. Here, we allow that the contact angle relation θ^ε involves a multivalued graph if the velocity of the contact line is zero. To still obtain a well-defined contact angle law, we reformulate the respective condition under the following assumption, which replaces (A5).

(A10) Restricted to $\mathbb{R} \setminus \{0\}$, θ^ε is a Lipschitz-continuous and strictly monotonic function into $(0, \pi)$. For a zero velocity, it can take any values as follow:

$$\theta^\varepsilon(0) \in \begin{cases} [\lim_{u \nearrow 0} \theta^\varepsilon(u), \lim_{u \searrow 0} \theta^\varepsilon(u)] & \text{if } \theta^\varepsilon \text{is increasing,} \\ [\lim_{u \searrow 0} \theta^\varepsilon(u), \lim_{u \nearrow 0} \theta^\varepsilon(u)] & \text{otherwise.} \end{cases}$$

Using the monotonicity of θ^ε, one can invert the relation with respect to the velocity. For this, let $\zeta^\varepsilon := (\cos(\theta^\varepsilon))^{-1}$ be the inverse of $\cos\theta^\varepsilon$. By (A10), ζ^ε is well-defined and Lipschitz-continuous. As before, we assume that ζ^ε depends regularly on ε.

(A11) ζ^ε has a uniform expansion

$$\zeta^\varepsilon(a) = \zeta^0(a) + \varepsilon\zeta^1(a) + \mathcal{O}(\varepsilon^2),$$

where $\zeta^0 : (-1,1) \to \mathbb{R}$ is Lipschitz-continuous.

With this, we study the Navier–Stokes system for two-phase flow Equations (15–25), but replace Equation (26) by the following, inverted contact angle condition:

$$\zeta^\varepsilon\Big(\boldsymbol{t}^\varepsilon_\Gamma\big|_{s=1} \cdot \boldsymbol{t}^\varepsilon_{\mathrm{w}}\big|_{x_1=\gamma_1^\varepsilon}\Big) = \partial_t\gamma_1^\varepsilon. \tag{97}$$

Since the analysis in Subsection 3.1 is independent of the interface region, and in particular does not use (A5) or the nonhysteretic contact angle equation (26), the derived bulk solutions given by Equations (49–52) remain unchanged.

Using (A1)–(A4), (A6)–(A8), and (A11) instead of (A5), we repeat the analysis close to the interface $\Gamma^\varepsilon(t)$ from Subsection 3.2. Following the same steps, we obtain a circular interface with constant curvature K^0, which is then implicitly given by

$$\partial_t\gamma_1^0 = \zeta^0\big(w^0(\gamma_1^0)K^0\big).$$

Combining this, the pressure Equation (77), and the outer pressure solution Equations (50, 52), one obtains

$$\partial_t\gamma_1^0 = \zeta^0\left(w^0(\gamma_1^0)\overline{\mathrm{Ca}}\left(p^0_{\mathrm{in}} - qJ(\gamma_1^0)\right)\right), \tag{98}$$

where

$$J(\gamma_1^0) := \int_0^{\gamma_1^0} \frac{3}{(w^0(x_1))^2(3\lambda^0 + w^0(x_1))}dx_1 + \int_{\gamma_1^0}^1 \frac{3\mathrm{M}}{(w^0(x_1))^2(3\lambda^0 + w^0(x_1))}dx_1.$$

Together with Equation (80), this forms a differential algebraic system of two equations for the two unknowns γ_1^0 and either p^0_{in} or q. Furthermore, the Stokes problem for finding the velocity close to the interface remains unchanged as well.

The solution process depends again on the chosen inlet boundary condition, analogously to the discussion in Subsection 3.2. As before, it is sufficient to obtain γ_1^0, p^0_{in}, and q, since these are the unknown coefficients for the bulk solutions $\boldsymbol{u}^0_m$ and p^0_m ($m \in \{\mathrm{I}, \mathrm{II}\}$) given by Equations (49–52). For an inlet velocity boundary condition $\boldsymbol{u}^\varepsilon_{\mathrm{I}} = \boldsymbol{u}^\varepsilon_{\mathrm{in}}$ (at $\Gamma^\varepsilon_{\mathrm{in}}$), the value of q is given. Hence, plugging this into Equation (80) yields γ_1^0, and thus one can solve Equation (98) for p^0_{in}. However, the solution of the inlet pressure p^0_{in} is not unique if the contact angle relation θ^ε is multivalued at velocity $u = 0$. On the other hand, for an inlet pressure condition $p^\varepsilon_{\mathrm{I}} = p^\varepsilon_{\mathrm{in}}$, the value of p^0_{in} is known. Then, the differential algebraic system of Equations (80,98) has index 1 and can be solved for q and γ_1^0. Inserting Equation (80) into Equation (98) and applying the implicit function

theorem to find q depending on γ_1^0, a sufficient condition for solvability is

$$(\zeta^0)' \left(w^0(\gamma_1^0)\overline{\mathrm{Ca}} \left(p_0^{\mathrm{in}} - qJ(\gamma_1^0) \right) \right) \neq \frac{1}{\overline{\mathrm{Ca}}(w^0(\gamma_1^0))^2 J(\gamma_1^0)}.$$

4 | AVERAGED MODELS AND EFFECTIVE QUANTITIES

Based on the asymptotic solution for pressures and velocities, we continue with the study of averaged models and effective quantities. First, we show that a local, one-dimensional version of Darcy's law holds for the transversally averaged pressures and velocities. In the second part, we derive effective quantities based on volume averages. The main result is a capillary pressure–saturation relationship involving dynamic effects.

In the following, we are only interested in the leading order relations. To simplify the notation, we therefore drop the indices $(\cdot)^\varepsilon$ and $(\cdot)^0$, and neglect higher-order terms. Hence, all following equations should be understood as up to terms of order ε.

4.1 | Transversal average: Darcy's law

In the following, we derive the transversal average of the quantities to demonstrate that the one-dimensional description of the thin strip yields a local version of Darcy's law. To this end, recall that the total flux (in the half strip) $q(t)$ is independent of x_1 as discussed in Remark 2. The transversally averaged velocity in x_1-direction is therefore given by

$$\begin{aligned}\overline{u}(t,x_1) &:= \begin{cases} (w(x_1))^{-1} \int_0^{w(x_1)} u_{1,\mathrm{I}}(t,\boldsymbol{x}) dx_2 & \text{for } x_1 < \gamma_1(t), \\ (w(x_1))^{-1} \int_0^{w(x_1)} u_{1,\mathrm{II}}(t,\boldsymbol{x}) dx_2 & \text{for } x_1 > \gamma_1(t), \end{cases} \\ &= \frac{q(t)}{w(x_1)}.\end{aligned}$$

Since the pressures p_{I} and p_{II} are independent of x_2, we obtain for the transversally averaged pressures

$$\begin{aligned}\overline{p}_{\mathrm{I}}(t,x_1) &:= (w(x_1))^{-1} \int_0^{w(x_1)} p_{\mathrm{I}}(t,\boldsymbol{x}) dx_2 \\ &= p_{\mathrm{in}}(t) - q(t) \int_0^{x_1} \frac{3}{(w(\xi))^2(3\lambda + w(\xi))} d\xi \qquad \text{for } x_1 < \gamma_1(t), \\ \overline{p}_{\mathrm{II}}(t,x_1) &:= (w(x_1))^{-1} \int_0^{w(x_1)} p_{\mathrm{II}}(t,\boldsymbol{x}) dx_2 \\ &= q(t) \int_{x_1}^{1} \frac{3\mathrm{M}}{(w(\xi))^2(3\lambda + w(\xi))} d\xi \qquad \text{for } x_1 > \gamma_1(t).\end{aligned}$$

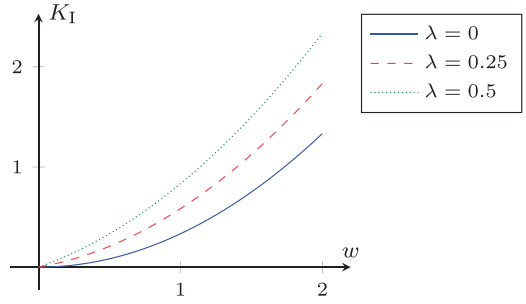

FIGURE 2 The local permeability K_I has a quadratic dependence on the width w and increases for increasing slip length λ

This means that the transversally averaged pressures satisfy a Darcy-type law

$$\overline{u}(t, x_1) = -K_m(x_1)\partial_{x_1}\overline{p}_m(t, x_1)$$

for $m \in \{\mathrm{I}, \mathrm{II}\}$, where the local permeabilities are given by

$$K_\mathrm{I}(x_1) := \frac{1}{3}w(x_1)(3\lambda + w(x_1)),$$

$$K_\mathrm{II}(x_1) := \frac{1}{3\mathrm{M}}w(x_1)(3\lambda + w(x_1)).$$

These permeabilities depend only on the local width w of the thin strip, on the slip length λ, and on the viscosity ratio M of the fluids (Figure 2). Note that this resembles the typical relation $\overline{u} = \frac{d^2}{12}\partial_{x_1}p$ for single-phase flow in a thin strip of diameter $d = 2w$. Also note that the permeabilities are nondimensional due to the chosen scaling of the x_2 coordinate by $\hat{w}(0)$ and the reference viscosity μ_I.

4.2 | Effective quantities: Dynamic capillary pressure

To obtain effective quantities such as the saturation and the intrinsically averaged pressures, we use volume averages. With these, we obtain a capillary pressure–saturation relationship involving dynamic effects. In line with classical volume averaging theory,[30,31] we define the volume average $\langle a_m \rangle$ of a quantity a_m defined in Ω_m, $m \in \{\mathrm{I}, \mathrm{II}\}$, to be

$$\langle a_m \rangle := \frac{\int_{\Omega_m} a_m d\boldsymbol{x}}{\int_\Omega d\boldsymbol{x}},$$

while the intrinsic average is

$$\langle a_m \rangle_m := \frac{\int_{\Omega_m} a_m d\boldsymbol{x}}{\int_{\Omega_m} d\boldsymbol{x}}.$$

The volume of the domain Ω_{I} is given by

$$\int_{\Omega_{\mathrm{I}}} d\boldsymbol{x} = \int_0^{\gamma_1} w(x_1)dx_1 = \mathcal{W}(\gamma_1).$$

Analogously, we have $\int_{\Omega} d\boldsymbol{x} = \mathcal{W}(1)$ and $\int_{\Omega_{\mathrm{II}}} d\boldsymbol{x} = \mathcal{W}(1) - \mathcal{W}(\gamma_1)$. Therefore, the saturation of fluid I is in leading order given by

$$S(t) := \langle 1_{\Omega_{\mathrm{I}}(t)} \rangle = \frac{\int_{\Omega_{\mathrm{I}}(t)} d\boldsymbol{x}}{\int_{\Omega} d\boldsymbol{x}} = \frac{\mathcal{W}(\gamma_1(t))}{\mathcal{W}(1)}. \tag{99}$$

Note that we only consider the case when both phases are present, so that $\gamma_1(t) \in (0,1)$ and $S \in (0,1)$. For simplicity, we define the function

$$\Psi(S) := \frac{1}{w(\mathcal{W}^{-1}(\mathcal{W}(1)S))}, \tag{100}$$

which represents the reciprocal of the local width depending on the saturation S and on the geometry of the thin strip. Note that the system of Equations (79–80) can be rewritten in terms of the saturation as

$$\begin{aligned} p_{\mathrm{in}} - q\mathcal{W}(1)\left(\int_0^S \frac{3(\Psi(\xi))^3}{3\lambda + (\Psi(\xi))^{-1}} d\xi + \int_S^1 \frac{3\mathrm{M}(\Psi(\xi))^3}{3\lambda + (\Psi(\xi))^{-1}} d\xi \right) \\ = \frac{\cos(\theta(\mathcal{W}(1)\Psi(S)\partial_t S))}{\overline{\mathrm{Ca}}} \Psi(S), \\ \partial_t S = \frac{q}{\mathcal{W}(1)}. \end{aligned}$$

However, this reformulation is less practical, since the function Ψ typically is not a closed-form expression.

Using Equation (50), the intrinsically averaged pressure of fluid I is

$$\langle p_{\mathrm{I}} \rangle_{\mathrm{I}} = \frac{1}{\mathcal{W}(\gamma_1)} \int_0^{\gamma_1} w(x_1) \left(p_{\mathrm{in}} - q \int_0^{x_1} \frac{3}{(w(\xi))^2(3\lambda + w(\xi))} d\xi \right) dx_1,$$

which can be rewritten after integration by parts as

$$\langle p_{\mathrm{I}} \rangle_{\mathrm{I}} = p_{\mathrm{I}}|_{x_1=\gamma_1} + \frac{3q}{\mathcal{W}(\gamma_1)} \int_0^{\gamma_1} \frac{\mathcal{W}(x_1)}{(w(x_1))^2(3\lambda + w(x_1))} dx_1. \tag{101}$$

Analogously, Equation (52) yields the intrinsically averaged pressure of fluid II to be

$$\langle p_{\mathrm{II}} \rangle_{\mathrm{II}} = p_{\mathrm{II}}|_{x_1=\gamma_1} - \frac{3\mathrm{M}q}{\mathcal{W}(1) - \mathcal{W}(\gamma_1)} \int_{\gamma_1}^1 \frac{\mathcal{W}(1) - \mathcal{W}(x_1)}{(w(x_1))^2(3\lambda + w(x_1))} dx_1. \tag{102}$$

Using Equation (79), the difference of the intrinsically averaged pressures, in the following called phase-pressure difference, is given by

$$\langle p_{\mathrm{I}}\rangle_{\mathrm{I}} - \langle p_{\mathrm{II}}\rangle_{\mathrm{II}} = \frac{\cos(\theta(\partial_t\gamma_1))}{\overline{\mathrm{Ca}}w(\gamma_1)} + 3q\left(\frac{1}{\mathcal{W}(\gamma_1)}\int_0^{\gamma_1}\frac{\mathcal{W}(x_1)}{(w(x_1))^2(3\lambda + w(x_1))}dx_1 + \frac{\mathrm{M}}{\mathcal{W}(1)-\mathcal{W}(\gamma_1)}\int_{\gamma_1}^{1}\frac{\mathcal{W}(1)-\mathcal{W}(x_1)}{(w(x_1))^2(3\lambda + w(x_1))}dx_1\right). \tag{103}$$

Using Equations (80,99,100), this difference can be expressed in the form

$$\langle p_{\mathrm{I}}\rangle_{\mathrm{I}} - \langle p_{\mathrm{II}}\rangle_{\mathrm{II}} = p_{c,\mathrm{loc}}(S,\partial_t S) + \tau(S)\partial_t S. \tag{104}$$

The first term on the right denotes the local capillary pressure $p_{c,\mathrm{loc}} := (p_{\mathrm{I}} - p_{\mathrm{II}})|_{x_1=\gamma_1}$ given by

$$p_{c,\mathrm{loc}}(S,\partial_t S) = \frac{\cos(\theta(\mathcal{W}(1)\Psi(S)\partial_t S))}{\overline{\mathrm{Ca}}}\Psi(S). \tag{105}$$

The second term in Equation (104) can be interpreted as a dynamic capillarity due to the viscous drag. In particular, its coefficient is

$$\tau(S) = \frac{3(\mathcal{W}(1))^2}{S}\int_0^S \frac{\xi(\Psi(\xi))^3}{3\lambda + (\Psi(\xi))^{-1}}d\xi + \frac{3(\mathcal{W}(1))^2\mathrm{M}}{1-S}\int_S^1 \frac{(1-\xi)(\Psi(\xi))^3}{3\lambda + (\Psi(\xi))^{-1}}d\xi, \tag{106}$$

which depends on the slip length λ, the viscosity ratio M, and the wall function w. Note that under static conditions, when $q \ll 1$, we have $p_{\mathrm{in}} \approx \langle p_{\mathrm{I}}\rangle_{\mathrm{I}} - \langle p_{\mathrm{II}}\rangle_{\mathrm{II}} = p_{c,\mathrm{loc}}$, such that the measurement of the inlet pressure yields (static) capillary pressure–saturation relation, but under the dynamic conditions studied here, these quantities can considerably differ. This one must be aware of when performing experiments.

The local capillary pressure $p_{c,\mathrm{loc}}$ depends reciprocally on the effective capillary number $\overline{\mathrm{Ca}}$ and on the local width $w(\mathcal{W}^{-1}(\mathcal{W}(1)S)) = 1/\Psi(S)$ of the thin strip. In case of a dynamic contact angle model of the form $\cos(\theta(u)) = \cos(\theta_s) + \eta\overline{\mathrm{Ca}}u$, the molecular kinetic theory in Refs. 68, 69, Equation (105) yields

$$p_{c,\mathrm{loc}}^{\mathrm{MKT}}(S,\partial_t S) = \frac{\cos(\theta_s)}{\overline{\mathrm{Ca}}}\Psi(S) + \eta\mathcal{W}(1)(\Psi(S))^2\partial_t S. \tag{107}$$

The static and dynamic effects are decoupled in this case. The first term models the static (local) capillary pressure, while the second term is a dynamic contribution.

In case of a constant contact angle $\theta \equiv \theta_s \in (0,\pi)$, Equation (105) yields the local capillary pressure

$$p_{c,\mathrm{loc}}^{\mathrm{const}}(S) = \frac{\cos(\theta_s)}{\overline{\mathrm{Ca}}}\Psi(S).$$

With $l(t) := \int_{\Gamma_{\boldsymbol{X}}(t)} ds$ being the length of the circular interface $\Gamma_{\boldsymbol{X}}(t)$ at time t, the local capillary pressure becomes

$$p_{c,\mathrm{loc}}^{\mathrm{const}}(l) = \frac{\frac{\pi}{2} - \theta_s}{\overline{\mathrm{Ca}}\,l}.$$

TABLE 2 Standard parameters for the thin strip of constant width

Parameter	Symbol	Value
Capillary number	$\overline{\mathrm{Ca}}$	1/2
Contact angle	θ	$\pi/3$
Slip length	λ	1/6
Viscosity ratio	M	1
Initial interface position	$\gamma_1\vert_{t=0}$	0
Inlet pressure	p_{in}	3

Observe that $l(t)$ can be assimilated to the interfacial area concept considered in Refs. 14, 15. Note that for a dynamic contact angle, there is no simple closed-form expression of the local capillary pressure as a function of the interface length (nor of its derivatives).

5 | NUMERICAL EXPERIMENTS

To illustrate the theoretical findings, we depict some numerical examples in this section. We start with a thin strip of constant width, and afterward consider a constricted "pore throat" with varying width. After a short discussion of the boundary conditions, we consider the resulting effective quantities. In particular, we study the effect of the slip length and the viscosity ratio and discuss the effect of a dynamic and a hysteretic contact angle model for both geometries.

We have implemented the numerical solutions using MATLAB® R2020a.[76] The source code is openly available under the CC-BY license in GitHub at https://github.com/s-lunowa/AsymptoticThinStripMCLSolver.[77]

5.1 | Thin strip of constant width

First we consider a simple case, which is a thin strip of constant width $w^\varepsilon \equiv 1$, and study the velocity and pressure distribution of the two phases as well as the movement of the interface. After a short discussion of the effect of different inlet boundary conditions, we will consider the effect of different parameter choices in the following subsections—the slip length in Subsection 5.1.1, the viscosity ratio in Subsection 5.1.2, and dynamic and hysteretic contact angle models in Subsections 5.1.3 and 5.1.4, respectively. Except for the varying parameter mentioned in each subsection, all the other ones are fixed, as given in Table 2. In particular, the contact angle model considered when discussing the other parameters is constant, that is, the contact angle is static and fluid I is nonwetting.

For this geometry, the solution given in Equations (49–52) for the bulk domains becomes

$$\boldsymbol{u}_{\mathrm{I}}(t,\boldsymbol{x}) = \begin{pmatrix} 3q(t)\frac{2\lambda+1-x_2^2}{6\lambda+2} \\ 0 \end{pmatrix}, \qquad p_{\mathrm{I}}(t,\boldsymbol{x}) = p_{\mathrm{in}}(t) - q(t)\frac{3x_1}{3\lambda+1}, \qquad \text{for } x_1 < \gamma_1(t), \tag{108}$$

$$\boldsymbol{u}_{\mathrm{II}}(t,\boldsymbol{x}) = \begin{pmatrix} 3q(t)\frac{2\lambda+1-x_2^2}{6\lambda+2} \\ 0 \end{pmatrix}, \qquad p_{\mathrm{II}}(t,\boldsymbol{x}) = q(t)\frac{3\mathrm{M}(1-x_1)}{3\lambda+1}, \qquad \text{for } x_1 > \gamma_1(t). \tag{109}$$

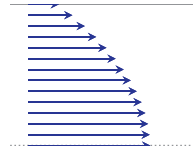

FIGURE 3 Velocity profile in the thin strip with constant width ($\lambda = 1/6$)

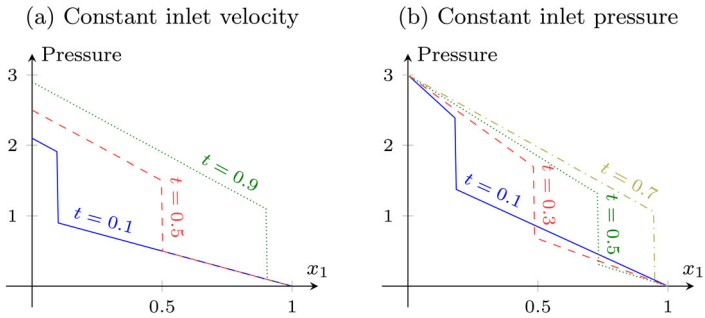

FIGURE 4 Pressure distribution over length x_1 at various times in the thin strip of constant width for viscosity ratio $\mathrm{M} = 0.5$. The solution depends on the inlet boundary condition and shows a more dynamic behavior in case (b) than in case (a)

This means that the velocity profiles are of Hagen–Poiseuille type (Figure 3). The pressures decrease linearly inside the bulk phases due to the viscous forces. Furthermore, the interface system of Equations (79,80) simplifies into

$$p_{\mathrm{in}}(t) - q(t)\frac{3\gamma_1(t) + 3\mathrm{M}(1-\gamma_1(t))}{3\lambda + 1} = \frac{\cos(\theta(q(t)))}{\mathrm{Ca}}, \quad \partial_t \gamma_1(t) = q(t). \tag{110}$$

The actual size of the quantities and the movement of the interface depend on the inlet boundary conditions, on the effective capillary number, on the slip length, on the viscosity ratio, and on the contact angle model. Here, we shortly discuss the qualitatively different cases with respect to the inlet boundary conditions and the viscosity ratio, when all other parameters are given by Table 2 for simplicity.

(a) When the inlet velocity is fixed, for example, $u_{\mathrm{in},1} = 4/3 - x_2^2$, one obtains $q(t) = 1$ and thus the constant (in time) velocities $u_{m,1} = 4/3 - x_2^2$ for $m \in \{\mathrm{I}, \mathrm{II}\}$, so that the interface moves linearly, $\gamma_1(t) = t$. The pressures are then given by

$$p_{\mathrm{I}}(t, \boldsymbol{x}) = 1 + 2\mathrm{M} + 2(1-\mathrm{M})t - 2x_1, \qquad p_{\mathrm{II}}(t, \boldsymbol{x}) = 2\mathrm{M}(1 - x_1).$$

For $\mathrm{M} \neq 1$, the pressure of fluid I is time-dependent, as depicted in Figure 4, while both pressures are constant in time for $\mathrm{M} = 1$.

(b) When the inlet pressure is fixed, for example, $p_{\mathrm{in}} = 3$, the flow of both fluids is time-dependent. For a viscosity ratio $\mathrm{M} < 1$, one obtains the solution

$$p_{\mathrm{I}}(t, \boldsymbol{x}) = 3 - \frac{2(1-\mathrm{M})x_1}{\sqrt{\mathrm{M}^2 + 2(1-\mathrm{M})t}}, \qquad p_{\mathrm{II}}(t, \boldsymbol{x}) = \frac{2\mathrm{M}(1-\mathrm{M})(1-x_1)}{\sqrt{\mathrm{M}^2 + 2(1-\mathrm{M})t}},$$

$$u_{m,1}(t, \boldsymbol{x}) = \frac{(1-\mathrm{M})\left(\frac{4}{3} - x_2^2\right)}{\sqrt{\mathrm{M}^2 + 2(1-\mathrm{M})t}}, \qquad \gamma_1(t) = \frac{\sqrt{\mathrm{M}^2 + 2(1-\mathrm{M})t} - \mathrm{M}}{1-\mathrm{M}},$$

for $m \in \{\mathrm{I}, \mathrm{II}\}$, shown in Figure 4. Analogous behavior can be observed when $\mathrm{M} > 1$. Only for $\mathrm{M} = 1$, both pressures are constant in time, like in (a).

From these examples, we observe a more dynamic behavior when the inlet pressure is given, which corresponds also to the typical setting for capillary pressure experiments. Thus, we restrict the following discussion to the case of given pressure boundary condition at the inlet.

Due to the constant width, the effective quantities have rather simple algebraic expressions. The saturation S coincides with the interface position, that is, $S = \gamma_1$. The local permeabilities are constant and given by

$$K_{\mathrm{I}} \equiv \frac{1+3\lambda}{3}, \qquad K_{\mathrm{II}} \equiv \frac{1+3\lambda}{3\mathrm{M}}. \tag{111}$$

The local capillary pressure, the dynamic coefficient and the phase-pressure difference are

$$p_{c,\mathrm{loc}}(S, \partial_t S) = \frac{\cos\theta(\partial_t S)}{\overline{\mathrm{Ca}}}, \tag{112}$$

$$\tau(S) = 3\frac{S + \mathrm{M}(1-S)}{6\lambda + 2}, \tag{113}$$

$$\langle p_{\mathrm{I}} \rangle_{\mathrm{I}} - \langle p_{\mathrm{II}} \rangle_{\mathrm{II}} = \frac{p_{\mathrm{in}} + p_{c,\mathrm{loc}}(S, \partial_t S)}{2}. \tag{114}$$

As direct consequence of the constant contact angle in Table 2, we obtain a constant local capillary pressure $p_{c,\mathrm{loc}} \equiv 1$ by Equation (112) and a constant phase-pressure difference $\langle p_{\mathrm{I}} \rangle_{\mathrm{I}} - \langle p_{\mathrm{II}} \rangle_{\mathrm{II}} \equiv 2$ by Equation (114). Changing the static contact angle $\theta \equiv \theta_s \in (0, \pi)$ or the capillary number $\overline{\mathrm{Ca}}$ influences the size of the local capillary pressure and the size of the phase-pressure difference in a straightforward way, while the behavior of the other quantities remains qualitatively the same. For simplicity, we do not discuss their detailed effects. Note that $p_{c,\mathrm{loc}}$ and $\langle p_{\mathrm{I}} \rangle_{\mathrm{I}} - \langle p_{\mathrm{II}} \rangle_{\mathrm{II}}$ do not depend on the slip length nor on the viscosity ratio. Hence, we only consider their behavior for dynamic and hysteretic contact angle models. Meanwhile, the dynamic coefficient depends on the slip length and the viscosity ratio, which is relevant in case of a inlet velocity condition.

5.1.1 | Effect of the slip length

First, we consider the effect of the slip length λ while using all other parameters as above. The velocity at the wall is given by

$$u_{m,1}\big|_{x_2=1} = q\frac{3\lambda}{3\lambda+1} \qquad \text{for } m \in \{\mathrm{I}, \mathrm{II}\}.$$

It is zero for $\lambda = 0$, increases for an increasing slip length, and approaches q for $\lambda \to \infty$, which corresponds to a total slip (Figure 5). This is a result of the decreased friction of the fluid at the wall for an increased slip length. In addition, this leads to a smaller dynamic coefficient τ, compare Equation (113) and Figure 5. For constant inlet pressure, the decrease of the pressure gradients in Equations (108,109) for an increased slip length λ are compensated by a larger total flux q, and thus a faster movement of the interface position γ_1 (Figure 5). The local permeabilities K_{I},

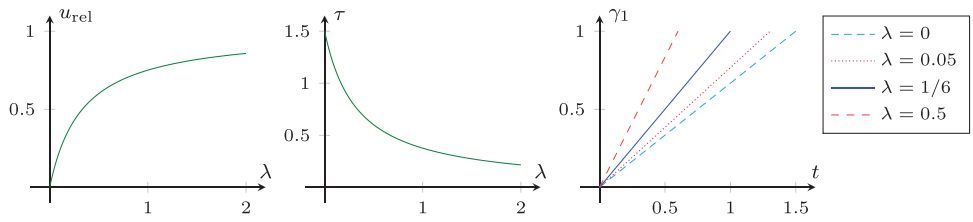

FIGURE 5 For an increasing slip length λ, the velocity ratio $u_{\text{rel}} = u_{m,1}|_{x_2=1}/q$ at the wall increases (left), while the dynamic parameter τ decreases (center). The interface position γ_1 moves faster for an increasing slip length λ (right)

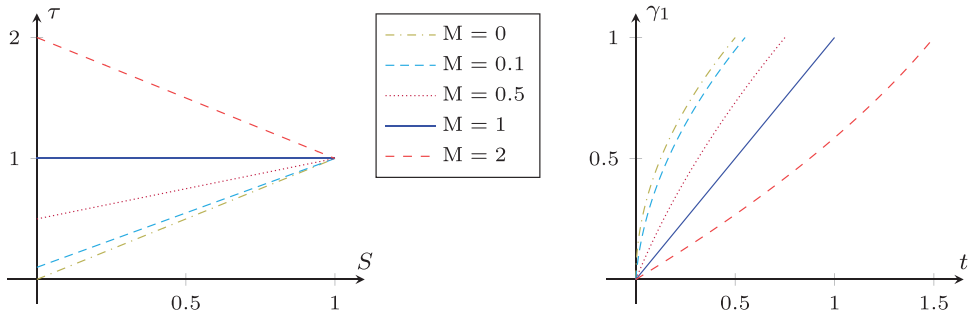

FIGURE 6 For increasing viscosity ratio M, the dynamic parameter τ increases (left), while the interface position γ_1 moves slower (right)

K_{II} show a similar behavior. Observe that since $w \equiv 1$, these only depend on the slip length. As follows from Equation (111) (cf. Figure 2), they increase linearly with λ.

5.1.2 | Effect of the viscosity ratio

Next, we continue the investigation for various viscosity ratios M. Since the viscous force in fluid II is proportional to the viscosity ratio M, the total flux q decreases when the viscosity ratio M increases (cf. Equation (110)). In particular, the interface position γ_1 moves faster when the thin strip is mainly filled by the less viscous fluid (Figure 6). Furthermore, we observe that the solutions converge for $\text{M} \to 0$ toward solution of the simplified, unsaturated flow model as discussed in Subsection 3.3. Note that we use $\gamma_1|_{t=0} = 10^{-3}$ when $\text{M} = 0$ to avoid the degeneration of the interface system in Equation (110).

The dynamic coefficient τ becomes larger for small saturations S, if the viscosity ratio is large ($\text{M} > 1$), and vice versa for $\text{M} < 1$ due to Equation (113), and shown in Figure 6. Note that one can observe even in this extremely simplified setting that the dynamic coefficient is saturation-dependent, except for fluids with the same viscosity ($\text{M} = 1$). In addition, the dynamic coefficient is monotonic in the saturation S for any viscosity ratio.

5.1.3 | Effect of a dynamic contact angle

Now, we consider the effect of a dynamic contact angle model. As we expect the similar qualitative behavior for different dynamic contact angle models, we restrict the discussion to the model

$$\theta(u) = \arccos(\max(\min(\cos(\theta_s) + \eta\overline{\text{Ca}}u, 1), -1)), \tag{115}$$

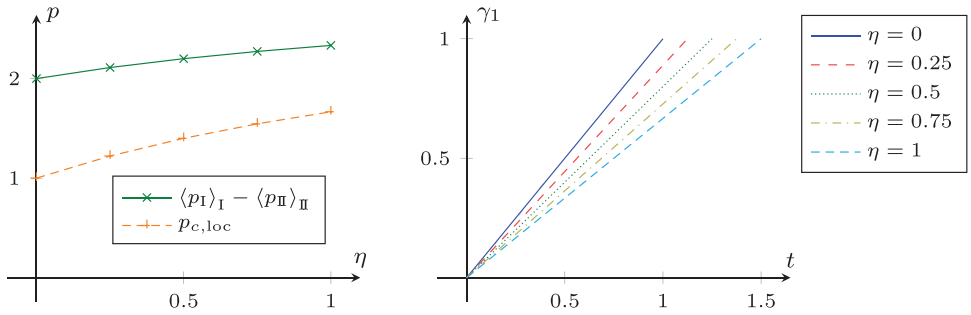

FIGURE 7 The local capillary pressure $p_{c,\mathrm{loc}}$ increases for increasing dynamic contact angle coefficient η (left). Hence, the movement of the interface position γ_1 slows down (right)

which is the linearized molecular kinetic theory model (for small velocities) from Refs. 47,55 68,69,73,74 restricted to the possible range $[0, \pi]$. Here, the parameter $\eta \geq 0$ models the effective friction at the contact point leading to a dynamic contact angle. For comparability, we fix the static contact angle $\theta_s = \pi/3$ and all the other parameters as in Table 2. Note that for any $\eta \geq 0$, the differential algebraic system in Equation (110) has a unique solution, since cosine is monotonic decreasing on $[0, \pi]$.

In contrast to the previous examples, the dynamic contact angle model does not affect the dynamic coefficient τ, but has an impact on the local capillary pressure $p_{c,\mathrm{loc}}$ and the phase-pressure difference $\langle p_{\mathrm{I}}\rangle_{\mathrm{I}} - \langle p_{\mathrm{II}}\rangle_{\mathrm{II}}$. Recall that the local capillary pressure is given in this case by Equation (107). In particular, its dynamic part is proportional to the parameter η. Hence, the interface position γ_1 moves slower when the parameter η increases (Figure 7). Note that the total flux q is constant, so that γ_1 is linear in time. Since $\mathrm{M} = 1$, the local capillary pressure and the phase-pressure difference are constant over S, so that we only show the dependence on η in Figure 7.

5.1.4 | Effect of a hysteretic contact angle

Finally, we consider the effect of a hysteretic contact angle model and compare it to the static and dynamic ones. As before we use the dynamic contact angle model in Equation (115) with static contact angle $\theta_s = \pi/3$. For the hysteretic contact angle model, the advancing and receding contact angles (with respect to fluid I) are chosen $\theta_a = \pi/4$ and $\theta_r = 5\pi/12$, respectively. Together with the same dynamic contact angle model away from $u = 0$, this yields

$$\zeta(a) = \begin{cases} \frac{a-\cos(\theta_r)}{\eta \overline{\mathrm{Ca}}} & \text{if } a < \cos(\theta_r), \\ \frac{a-\cos(\theta_a)}{\eta \overline{\mathrm{Ca}}} & \text{if } a > \cos(\theta_a), \\ 0 & \text{otherwise.} \end{cases} \tag{116}$$

Recall that ζ is the inverse of $\cos\theta$. We consider a drainage and imbibition cycle by choosing the time-dependent inlet pressure $p_{\mathrm{in}}(t) = 3 - t$, and stop the simulations when the interface position returns to the inlet. The other parameters are taken from Table 2.

As in the dynamic case, we observe that the movement of the interface position γ_1 is slower when the parameter η is increased (Figure 8 (top)). While the total flux q is linear for the static

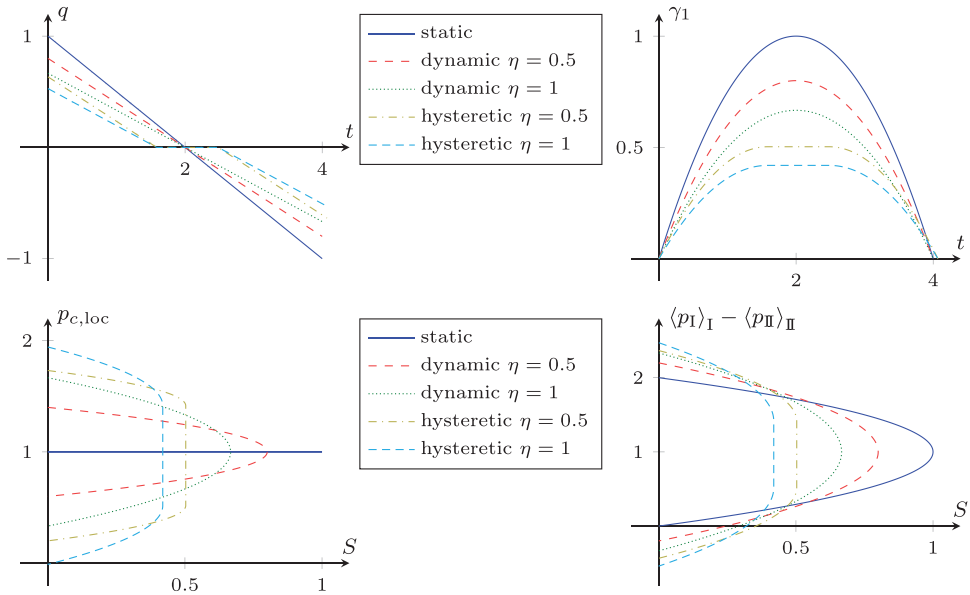

FIGURE 8 The total flux q (top-left) is linear for the static and dynamic contact angle model, while being zero for some time for the hysteretic model. The interface position γ_1 moves accordingly (top-right). In case of the hysteretic model, it is at rest, when the local capillary pressure $p_{c,\mathrm{loc}}$ (bottom-left) lies in between the (static) capillary pressures for drainage and imbibition, that is, $p_{c,\mathrm{loc}}$ is multivalued at the maximal reached saturation. For the dynamic models, $p_{c,\mathrm{loc}}$ at the maximal saturation is exactly the static capillary pressure. The phase-pressure difference $\langle p_\mathrm{I}\rangle_\mathrm{I} - \langle p_\mathrm{II}\rangle_\mathrm{II}$ (bottom-right) shows the same qualitative behavior

and dynamic contact angle model, so that γ_1 is quadratic in time, the hysteretic model leads to a constant interface position when $\theta_a \leq \theta \leq \theta_r$. Therefore, the local capillary pressure $p_{c,\mathrm{loc}}$ and the phase-pressure difference $\langle p_\mathrm{I}\rangle_\mathrm{I} - \langle p_\mathrm{II}\rangle_\mathrm{II}$ at the maximal reached saturation is multivalued taking all values between the (static) drainage and imbibition capillary pressures (Figure 8 (bottom)). On the other hand, for the dynamic contact angle model, $p_{c,\mathrm{loc}}$ and $\langle p_\mathrm{I}\rangle_\mathrm{I} - \langle p_\mathrm{II}\rangle_\mathrm{II}$ at the maximal saturation are given by the static capillary pressure, since $\partial_t S = 0$. Furthermore, the hysteresis leads to higher deviations from the static capillary pressure and thus a smaller maximal saturation. Finally, note that p_in is linear and reaches $p_{c,\mathrm{loc}}^{\mathrm{const}}$ at $t = 2$ such that all curves with the dynamic contact angle model are symmetric. Since θ_a and θ_r have the same distance from θ_s, the same holds in the hysteretic cases.

5.2 | Constricted "pore throat"

Next, we consider a strip with varying width

$$w(x_1) = 2/3 + \cos(2\pi x_1)/3,$$

which represents a constricted "pore throat." As before, we shortly discuss the velocity and pressure distribution of the two phases as well as the movement of the interface, before proceeding with the detailed discussion of the effect of the slip length, of the viscosity ratio, and of a dynamic

TABLE 3 Standard parameters for the case of varying width

Parameter	Symbol	Value
Capillary number	$\overline{\mathrm{Ca}}$	1/2
Contact angle	θ	$\pi/3$
Slip length	λ	1/6
Viscosity ratio	M	1
Initial interface position	$\gamma_1\vert_{t=0}$	0
Inlet pressure	p_{in}	12

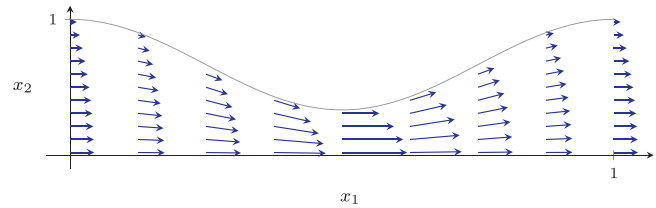

FIGURE 9 Velocity profile in the thin strip of varying width ($\lambda = 1/6$)

and a hysteretic contact angle model, varying each individually, while fixing all other parameters as given in Table 3. Note that we choose a static contact angle such that fluid I is nonwetting.

While the overall trend is similar to the previous case with constant width, we additionally observe here a strong impact of the geometry on the flow behavior and thus on the effective quantities. In contrast to the constant-width case, the local capillary pressure $p_{c,\mathrm{loc}}$ now depends on the saturation due to the constriction (Figure 11). Analogously, the phase-pressure difference $\langle p_{\mathrm{I}}\rangle_{\mathrm{I}} - \langle p_{\mathrm{II}}\rangle_{\mathrm{II}}$ varies in the saturation.

The solution in the bulk domains given by Equations (49–52) for this geometry then reads

$$u_{m,1}(t,\boldsymbol{x}) = 9q(t)\frac{(c(x_1))^2 + 5c(x_1) + 6 - x_2^2}{(c(x_1)+2)^2(2c(x_1)+7)},$$

$$u_{m,2}(t,\boldsymbol{x}) = \varepsilon 18\pi q(t)\sin(2\pi x_1)\left(\frac{18(c(x_1)+3)x_2^3}{(c(x_1)+2)^3(2c(x_1)+7)^2} - \frac{(2(c(x_1))^2 + 12c(x_1)+19)x_2}{(c(x_1)+2)^2(2c(x_1)+7)^2}\right)$$

for $m \in \{\mathrm{I}, \mathrm{II}\}$, where $c(x_1) := \cos(2\pi x_1)$, shown in Figure 9, while

$$p_{\mathrm{I}}(t,\boldsymbol{x}) = \frac{3}{2+c(\gamma_1(t))} + \frac{9q(t)\sin(2\pi x_1)}{\pi(c(x_1)+2)} + \frac{24q(t)\left(\pi H(0.5-x_1) - \arctan\left(\frac{\sqrt{5}}{3}\tan(\pi x_1)\right)\right)}{\pi\sqrt{5}},$$

for $x_1 < \gamma_1(t)$, and

$$p_{\mathrm{II}}(t,\boldsymbol{x}) = \frac{9q(t)\sin(2\pi x_1)}{\pi(c(x_1)+2)} + \frac{24q(t)\left(\pi H(0.5-x_1) - \arctan\left(\frac{\sqrt{5}}{3}\tan(\pi x_1)\right)\right)}{\pi\sqrt{5}}$$

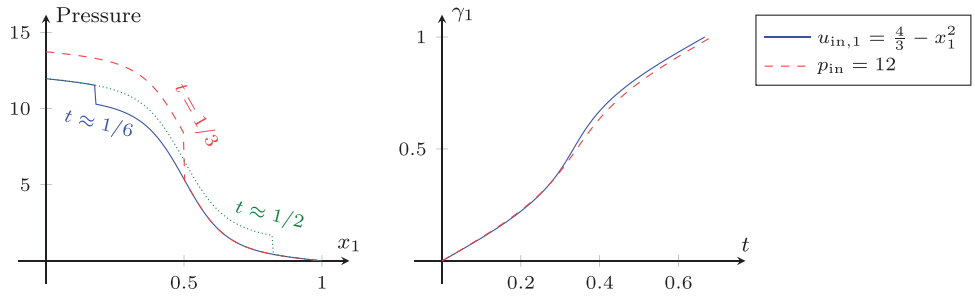

FIGURE 10 Pressure distribution over length x_1 at various times (left) for fixed inlet velocity $u_{\text{in},1} = 4/3 - x_1^2$ and interface position γ_1 over time t (right) for fixed inlet velocity $u_{\text{in},1} = 4/3 - x_1^2$ and fixed pressure condition $p_{\text{in}} = 12$ in the thin strip of varying width

for $x_1 > \gamma_1(t)$, where H denotes the Heaviside graph (Figure 10). The first velocity component is higher where the width is reduced, while the second component adjusts to the changes in width to maintain the incompressibility (Figure 9). Note that the second velocity component is of order ε due to the different scaling. Accordingly, the pressure gradients depend on the local width and are steeper around the constriction in the middle. This leads to the s-shaped pressure profiles instead of the linear ones in the constant-width case.

For fixed inlet velocity $u_{\text{in},1} = 4/3 - x_2^2$, that is, for $q \equiv 1$, the pressure solutions at several times are depicted in Figure 10 together with the evolution of the interface position $\gamma_1(t)$, which is given implicitly by $t = 2\gamma_1(t)/3 + \sin(2\pi\gamma_1(t))/(6\pi)$. Note that the interface position γ_1 moves faster in the vicinity of the constriction, since the average velocity $\overline{u} = q/w$ is higher around the constriction (cf. Figure 9). Furthermore, the movement is very similar to the one obtained with constant inlet pressure $p_{\text{in}} \equiv 12$. Hence, we restrict the following discussion to this inlet pressure condition. Note that this larger inlet pressure is necessary to obtain a similar total flux as in the constant-width case, since the width is reduced.

For this geometry, we still can derive relations for the effective quantities obtained in Subsection 4.2. We obtain for the saturation

$$S = \gamma_1 + \frac{1}{4\pi}\sin(2\pi\gamma_1), \qquad \partial_t S = \frac{3}{2}q.$$

Since this function $S(\gamma_1)$ has no analytical inverse, there is no closed-form expression for the local capillary pressure $p_{c,\text{loc}}$ Equation (105) nor for the dynamic coefficient τ Equation (106). Their numeric approximations are depicted in Figure 11. Both have a peak at $S = 0.5$, where the interface passes the position $x_1 = 0.5$ with the smallest width. For the local capillary pressure, this results from the reciprocal dependence on the local width, while the dynamic coefficient is symmetric due to the symmetric wall and the viscosity ratio $M = 1$. Note that the dynamic effects are much stronger than in the constant-width setting due to the reduced width, which requires larger pressure gradients to maintain the flow. Hence, we conclude that the wall shape has a significant impact, especially on the dynamic effects.

5.2.1 | Effect of the slip length

We begin the investigation for various slip lengths λ. As in the previous, constant-width case, the movement of the interface position γ_1 is faster when the slip length is increased. However, the

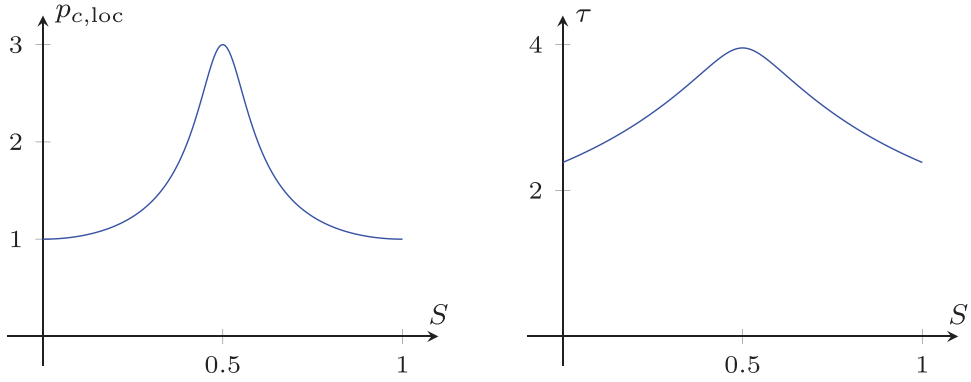

FIGURE 11 The local capillarity pressure $p_{c,\mathrm{loc}}$ increases for saturations below $S = 0.5$, and decreases thereafter (left). The dynamic coefficient τ shows an analogous behavior (right). This is a result of the symmetric constriction of the thin strip

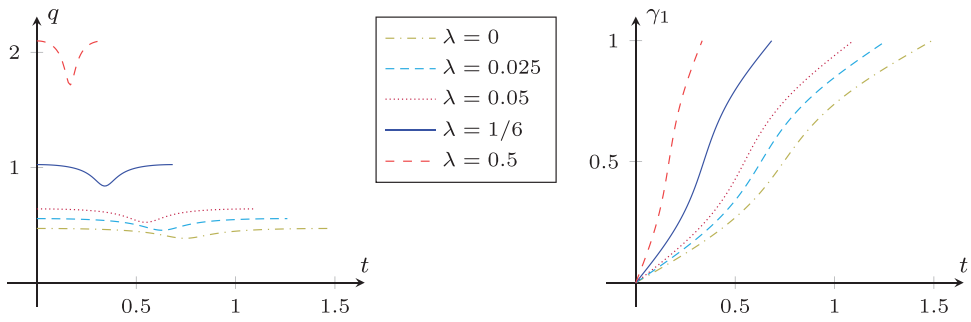

FIGURE 12 The total flux q is drastically reduced while the interface passes through the constriction due to the larger capillary pressure (left). It increases when the slip length λ is increased, so that the movement of the interface position γ_1 is faster (right)

total flux q is drastically reduced while the interface passes through the constriction due to the higher capillary pressure (Figure 12).

The dynamic coefficient τ is lower when the slip length increases as shown in Figure 13. In contrast to the constant-width case, it is nonmonotonic in the saturation, and maximal around $S = 0.5$, that is, when the interface passes through the constriction around $x_1 = 0.5$. Note that the combination of higher velocity with lower dynamic coefficient leads to almost no changes in the phase-pressure difference $\langle p_{\mathrm{I}} \rangle_{\mathrm{I}} - \langle p_{\mathrm{II}} \rangle_{\mathrm{II}}$ for all slip lengths (Figure 13).

5.2.2 | Effect of the viscosity ratio

Next, we consider the effect of the viscosity ratio M. As in the previous, constant-wall case, the total flux q is smaller when the viscosity ratio M increases (Figure 14). Especially at early times t, one can observe large total fluxes q, when the viscosity ratio is very small ($\mathrm{M} \leq 0.1$), since the strip is filled with the extremely mobile fluid II. On the other hand, the total flux is reduced while the interface passes through the constriction, but this effect is very small compared to the effect of viscosity for $\mathrm{M} < 1$. As before, the solutions converge for $\mathrm{M} \to 0$ toward the simplified, unsat-

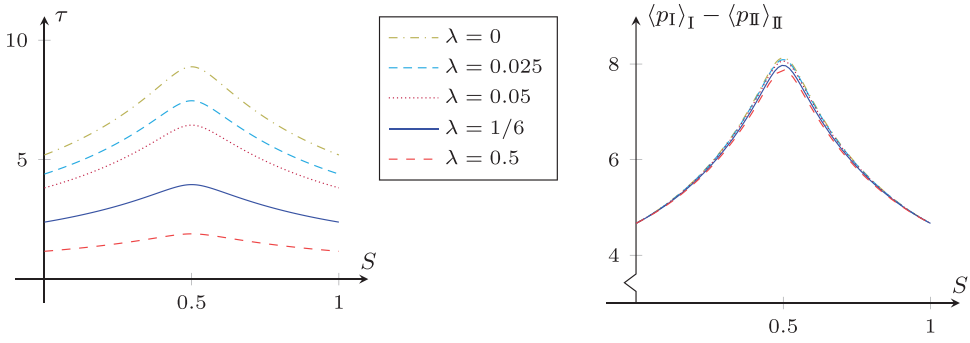

FIGURE 13 The dynamic coefficient τ decreases for increasing slip length λ (left). It is nonmonotonic in the saturation. The resulting phase-pressure difference $\langle p_{\mathrm{I}}\rangle_{\mathrm{I}} - \langle p_{\mathrm{II}}\rangle_{\mathrm{II}}$ is also nonmonotonic, but almost the same for all slip lengths (right)

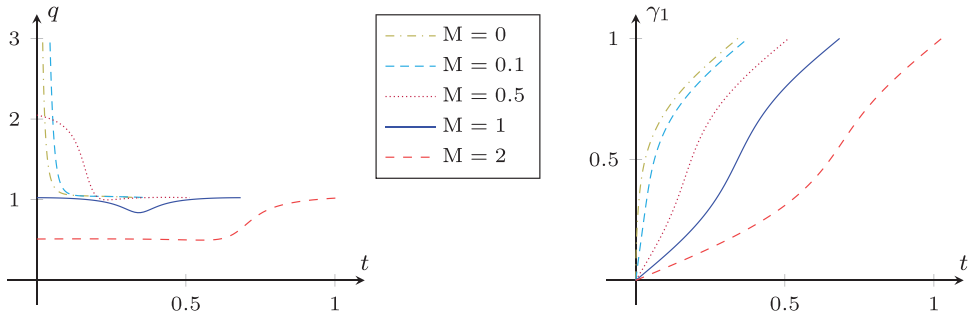

FIGURE 14 The total flux q is high when the thin strip is mainly filled with the less viscous fluid (left). It is smaller while the interface passes through the constriction. When the viscosity ratio M is increased, the interface position γ_1 moves generally slower (right)

urated flow model as discussed in Subsection 3.3 (cf. Figure 14). Note that we use $\gamma_1|_{t=0} = 10^{-3}$ when $\mathrm{M} = 0$ to avoid the degeneration of the interface system of Equations (79,80).

The dynamic coefficient τ becomes larger for small saturations S, if the viscosity ratio is larger ($\mathrm{M} > 1$), and vice versa for $\mathrm{M} < 1$, as shown in Figure 15. The rapid change close to $S = 0.5$ is due to the strong influence of the region around $x_1 = 0.5$, where the thin strip has its minimal width. Note that for small viscosity ratio $\mathrm{M} \leq 0.1$ and saturation below 0.4, the dynamic coefficient is almost zero. Furthermore, we observe here nonmonotonic behavior of the dynamic coefficient τ for every viscosity ratio, while it is monotonic in the constant-width case. This is due to the interplay between the constricted geometry and the nonlinear dynamic effect given by Equation (106). Finally, note that the combination of higher velocity with lower dynamic coefficient leads to almost no changes in the phase-pressure difference $\langle p_{\mathrm{I}}\rangle_{\mathrm{I}} - \langle p_{\mathrm{II}}\rangle_{\mathrm{II}}$ for all moderate viscosity ratios (Figure 15). Only for a very small viscosity ratio $\mathrm{M} \leq 0.1$, the phase-pressure difference is slightly lower for saturations between 0 and 0.5.

5.2.3 | Effect of a dynamic contact angle

We consider the effect of a dynamic contact angle model. As for the constant-width case, we use Equation (115) with $\theta_s = \pi/3$. The total flux q is smaller when η is increased (Figure 16). This effect is amplified while the interface passes through the constriction.

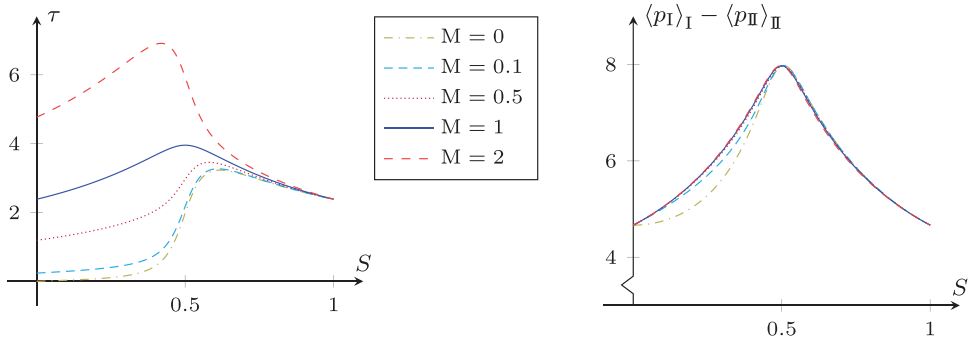

FIGURE 15 The dynamic parameter τ increases for increasing viscosity ratio M (left). It is nonmonotonic in the saturation. The resulting phase-pressure difference $\langle p_{\mathrm{I}}\rangle_{\mathrm{I}} - \langle p_{\mathrm{II}}\rangle_{\mathrm{II}}$ is also nonmonotonic, but almost the same for all moderate viscosity ratios (right)

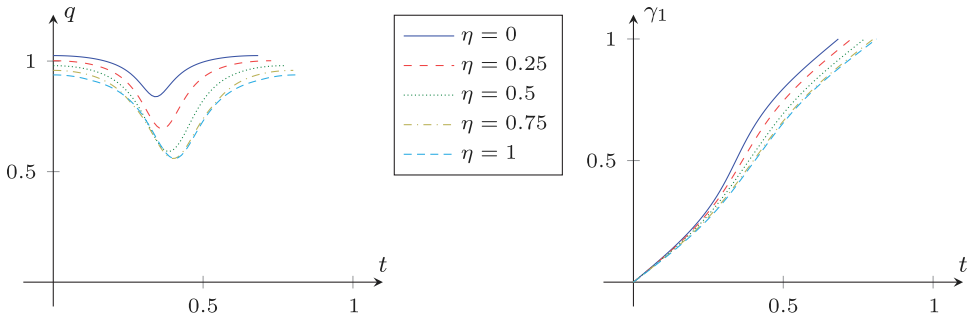

FIGURE 16 The total flux q decreases for higher values of η, since the (dynamic) local capillary pressure increases (left). Accordingly, the interface position γ_1 moves slower (right). Due to the constriction, the effect is maximal for $\gamma_1 = 0.5$

Although the total flux is smaller, the local capillary pressure $p_{c,\mathrm{loc}}$ and the phase-pressure difference $\langle p_{\mathrm{I}}\rangle_{\mathrm{I}} - \langle p_{\mathrm{II}}\rangle_{\mathrm{II}}$ increase for increasing η (Figure 17). The maximum is attained at $S = 0.5$, when the interface passes the minimal width. There, the dynamic effect is also the highest. Note that the curves for $\eta = 0.75$ and $\eta = 1$ partly coincide because the dynamic contact angle reaches π in both cases. In a laboratory experiment, this could lead to instabilities and the formation of bubbles or a thin residual film. However, that such behavior is beyond the scope of the model presented here.

5.2.4 | Effect of a hysteretic contact angle

Finally, we consider the effect of a hysteretic contact angle model and compare it to the static and dynamic ones. As in the constant-width case, we use the dynamic contact angle model in Equation (115) with $\theta_s = \pi/3$ and the hysteretic contact angle model in Equation (116) with $\theta_a = \pi/4$ and $\theta_r = 5\pi/12$. We consider a drainage and imbibition cycle by choosing the time-dependent inlet pressure $p_{\mathrm{in}}(t) = 9 - 4t$, and stop the simulations when the interface position returns to the inlet. The other parameters are taken from Table 3.

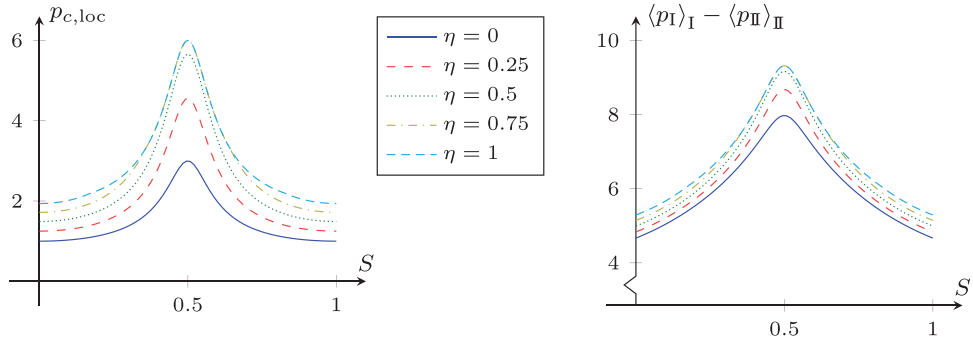

FIGURE 17 The local capillary pressure $p_{c,\mathrm{loc}}$ increases for increasing dynamic contact angle coefficient η (left). It attains its maximum at $S = 0.5$, when the interface passes the minimal width. The resulting phase-pressure difference $\langle p_{\mathrm{I}} \rangle_{\mathrm{I}} - \langle p_{\mathrm{II}} \rangle_{\mathrm{II}}$ shows the same behavior (right)

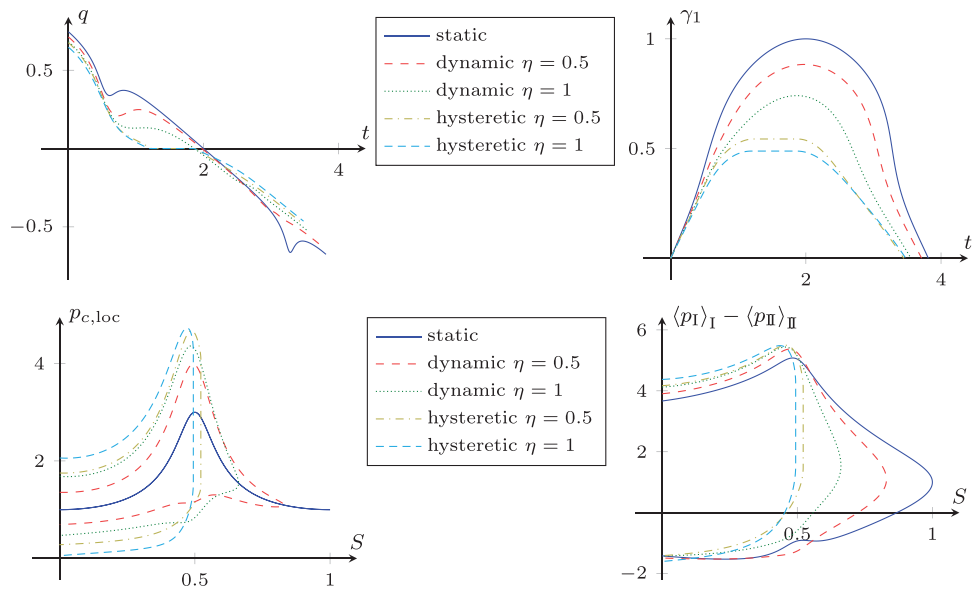

FIGURE 18 The total flux q (top-left) decreases faster when the interface passes through the constriction. In case of the hysteretic contact angle model, the interface position γ_1 (top-right) stops in the constriction when the local capillary pressure $p_{c,\mathrm{loc}}$ (bottom-left) lies in between the (static) capillary pressures for drainage and imbibition, whereas $p_{c,\mathrm{loc}}$ at the maximal saturation is exactly the static capillary pressure for the dynamic models. The phase-pressure difference $\langle p_{\mathrm{I}} \rangle_{\mathrm{I}} - \langle p_{\mathrm{II}} \rangle_{\mathrm{II}}$ (bottom-right) shows the same qualitative behavior

As before, the total flux q decreases faster, when the interface passes through the constriction (Figure 18 (top)). Note that the higher capillary pressure when passing the constriction counteracts the drainage, while it increases the imbibition speed. This results in a more negative velocity. In case of the hysteretic contact angle model, the interface position γ_1 stops in the constriction, while the pressure lies in between the (static) capillary pressures for drainage and imbibition, so that the local capillary pressure $p_{c,\mathrm{loc}}$ and the phase-pressure difference $\langle p_{\mathrm{I}} \rangle_{\mathrm{I}} - \langle p_{\mathrm{II}} \rangle_{\mathrm{II}}$ are multivalued at the maximal saturation. In contrast, the dynamic model yields a direct switching between drainage and imbibition, when $p_{c,\mathrm{loc}}$ is exactly the static capillary pressure (at the maximal

saturation) (Figure 18 (bottom)). Hence, hysteresis also leads to higher deviations from the static capillary pressure and thus a smaller maximal saturation.

6 | CONCLUSION

We have formally derived the asymptotic solution for the flow of two immiscible fluids in a two-dimensional thin strip of varying width, where the fluid–fluid interface is treated as a free boundary. The obtained effective models form a system of differential algebraic equations for the interface position and the total flux, and are applicable to a wide range of viscosity ratios M, of slip lengths λ, as well as contact angle models. The resulting effective relations are a Darcy-type equation for the local flow, and a capillary pressure–saturation relationship involving dynamic effects.

We have discussed the effects of a varying pore width, of the viscosity ratio, of the slip length as well as of having a dynamic and a hysteretic contact angle law through numerical experiments. In particular, the results for a varying pore width show that the geometry has a large influence on the effective quantities and their behavior. While dynamic effects occur even for a static contact angle model, hysteresis in the capillary pressure is only present when a hysteretic contact model is used.

The presented models and effective relations can be generalized to asymmetric as well as tube-like three-dimensional domains with heterogeneities in the contact angle. Furthermore, rough walls of type $w^\varepsilon(x_1) = w(x_1) + \varepsilon w^1(x_1/\varepsilon) + \mathcal{O}(\varepsilon)$ would strongly affect the shape and position of the interface. This needs to be investigated in the future. In addition, it remains to validate the effective models by a direct comparison with numerical simulations of the full model or with experiments in single pores. Our future work will focus on the radial-symmetric case in three dimensions including the effect of outer forces such as gravity. Such three-dimensional models can be further used in pore-network models or for upscaling in a bundle-of-tubes model.

ACKNOWLEDGMENTS

We thank Arjen Mascini, Tom Bultreys, and Veerle Cnudde for the helpful comments and discussions. This work was funded by the Hasselt University (project BOF17NI01) and the Research Foundation Flanders (FWO, projects G051418N and G0G1316M). We thank the Deutsche Forschungsgemeinschaft (DFG, German Research Foundation) for supporting this work by funding SFB 1313, Project Number 327154368.

ORCID

Stephan B. Lunowa https://orcid.org/0000-0002-5214-7245
Carina Bringedal https://orcid.org/0000-0003-0495-2634
Iuliu Sorin Pop https://orcid.org/0000-0001-9647-4347

REFERENCES

1. Darcy HPG., *Les Fontaines publiques de la ville de Dijon. Exposition et application des principes à suivre et des formules à employer dans les questions de distribution d'eau, etc.* Paris: V. Dalmont; 1856.
2. Richards LA. Capillary conduction of liquids through porous mediums. *Physics*. 1931;1:318-333.
3. Morrow NR, Harris CC. Capillary equilibrium in porous materials. *Soc Pet Eng J*. 1965;5:15-24. https://doi.org/10.2118/1011-PA
4. Glass RJ, Steenhuis TS, Parlange J-Y. Mechanism for finger persistence in homogeneous, unsaturated, porous media: theory and verification. *Soil Sci*. 1989;148:60-70.

5. Shiozawa S, Fujimaki H. Unexpected water content profiles under flux-limited one-dimensional downward infiltration in initially dry granular media. *Water Resour Res*. 2004;40:W07404. https://doi.org/10.1029/2003WR002197
6. DiCarlo DA. Experimental measurements of saturation overshoot on infiltration. *Water Resour Res*. 2004;40:W04215.
7. Bottero S, Hassanizadeh SM, Kleingeld PJ, Heimovaara TJ. Nonequilibrium capillarity effects in two-phase flow through porous media at different scales. *Water Resour Res*. 2011;47:W10505.
8. Zhuang L, Hassanizadeh SM, Qin C-Z, de Waal A. Experimental investigation of hysteretic dynamic capillarity effect in unsaturated flow. *Water Resour Res*. 2017;53:9078-9088. https://doi.org/10.1002/2017WR020895
9. Parker JC, Lenhard RJ. A model for hysteretic constitutive relations governing multiphase flow: 1. Saturation-pressure relations. *Water Resour Res*. 1987;23:2187-2196. https://doi.org/10.1029/WR023i012p02187
10. Beliaev AY, Hassanizadeh SM. A theoretical model of hysteresis and dynamic effects in the capillary relation for two-phase flow in porous media. *Transp Porous Med*. 2001;43:487-510.
11. Beliaev AY, Schotting RJ. Analysis of a new model for unsaturated flow in porous media including hysteresis and dynamic effects. *Comput Geosci*. 2001;5:345-368.
12. Beljadid A, Cueto-Felgueroso L, Juanes R. A continuum model of unstable infiltration in porous media endowed with an entropy function. *Adv Water Resour*. 2020;144:103684. https://doi.org/10.1016/j.advwatres.2020.103684
13. Schweizer B. Hysteresis in porous media: modelling and analysis. *Interfaces Free Bound*. 2017;19:417-447.
14. Hassanizadeh SM, Gray WG. Thermodynamic basis of capillary pressure in porous media. *Water Resour Res*. 1993;29:3389-3405. https://doi.org/10.1029/93WR01495
15. Hassanizadeh SM, Gray WG. Toward an improved description of the physics of two-phase flow. *Adv Water Resour*. 1993;16:53-67.
16. Hilfer R. Capillary pressure, hysteresis and residual saturation in porous media. *Physica A*. 2006;359:119-128. https://doi.org/10.1016/j.physa.2005.05.086
17. Hilfer R. Macroscopic capillarity and hysteresis for flow in porous media. *Phys Rev E*. 2006;73:016307.
18. Hilfer R. Macroscopic capillarity without a constitutive capillary pressure function. *Physica A*. 2006;371:209-225. https://doi.org/10.1016/j.physa.2006.04.051
19. van Duijn CJ, Fan Y, Peletier LA, Pop IS. Travelling wave solutions for degenerate pseudo-parabolic equations modelling two-phase flow in porous media. *Nonlinear Anal Real World Appl*. 2013;14:1361-1383. https://doi.org/10.1016/j.nonrwa.2012.10.002
20. van Duijn CJ, Mitra K. Hysteresis and horizontal redistribution in porous media. *Transp Porous Media*. 2018;122:375-399. https://doi.org/10.1007/s11242-018-1009-2
21. Mitra K, van Duijn CJ. Wetting fronts in unsaturated porous media: the combined case of hysteresis and dynamic capillary pressure. *Nonlinear Anal Real World Appl*. 2019;50:316-341. https://doi.org/10.1016/j.nonrwa.2019.05.005
22. Doster F, Zegeling PA, Hilfer R. Numerical solutions of a generalized theory for macroscopic capillarity. *Phys Rev E*. 2010;81:036307.
23. Lamacz A, Rätz A, Schweizer B. A well-posed hysteresis model for flows in porous media and applications to fingering effects. *Adv Math Sci Appl*. 2011;21:33-64.
24. Hilfer R, Doster F, Zegeling PA. Nonmonotone saturation profiles for hydrostatic equilibrium in homogeneous porous media. *Vadose Zone J*. 2012;11:1-6. https://doi.org/10.2136/vzj2012.0021
25. Koch J, Rätz A, Schweizer B. Two-phase flow equations with a dynamic capillary pressure. *Eur J Appl Math*. 2013;24:49-75. https://doi.org/10.1017/S0956792512000307
26. Rätz A, Schweizer B. Hysteresis models and gravity fingering in porous media. *Z Angew Math Mech*. 2014;94:645-654. https://doi.org/10.1002/zamm.201200052
27. Zhuang L, Hassanizadeh SM, van Duijn C, Zimmermann S, Zizina I, Helmig R. Experimental and numerical studies of saturation overshoot during infiltration into a dry soil. *Vadose Zone J*. 2019;18:1-13. https://doi.org/10.2136/vzj2018.09.0167
28. Cushman JH, Bennethum LS, Hu BX. A primer on upscaling tools for porous media. *Adv Water Resour*. 2002;25:1043-1067. https://doi.org/10.1016/S0309-1708(02)00047-7
29. Hassanizadeh SM, Gray WG. General conservation equations for multi-phase systems: 1. Averaging procedure. *Adv Water Resour*. 1979;2:131-144.

30. Whitaker S. Flow in porous media II: the governing equations for immiscible, two-phase flow. *Transp Porous Media*. 1986;1:105-125.
31. Quintard M, Whitaker S. Two-phase flow in heterogeneous porous media: the method of large-scale averaging. *Transp Porous Media*. 1988;3:357-413. https://doi.org/10.1007/BF00233177
32. Hornung U., *Homogenization and Porous Media*. New York: Springer; 1997.
33. Auriault J. Nonsaturated deformable porous media: quasistatics. *Transp Porous Media*. 1987;2:45-64. https://doi.org/10.1007/BF00208536
34. Allaire G. Homogenization of the stokes flow in a connected porous medium. *Asymptotic Anal*. 1989;2:203-222. https://doi.org/10.3233/ASY-1989-2302
35. Allaire G. Homogenization of the Navier-Stokes equations with a slip boundary condition. *Commun Pure Appl Math*. 1991;44:605-641. https://doi.org/10.1002/cpa.3160440602
36. Mikelić A. Homogenization of nonstationary Navier-Stokes equations in a domain with a grained boundary. *Ann Mat Pura Appl*. 1991;158:167-179.
37. Mikelić A, Paoli L. On the derivation of the Buckley-Leverett model from the two fluid Navier–Stokes equations in a thin domain. *Comput Geosci*. 1997;1:59-83. https://doi.org/10.1023/A:1011509010432
38. Mikelić A. On an averaged model for the 2-fluid immiscible flow with surface tension in a thin cylindrical tube. *Comput Geosci*. 2003;7:183-196. https://doi.org/10.1023/A:1025527716078
39. Sharmin S, Bringedal C, Pop IS. On upscaling pore-scale models for two-phase flow with evolving interfaces. *Adv Water Resour*. 2020;142:103646. https://doi.org/10.1016/j.advwatres.2020.103646
40. Picchi D, Battiato I. The impact of pore-scale flow regimes on upscaling of immiscible two-phase flow in porous media. *Water Resour Res*. 2018;54:6683-6707. https://doi.org/10.1029/2018WR023172
41. van Noorden TL. Crystal precipitation and dissolution in a thin strip. *Eur J Appl Math*. 2009;20:69-91. https://doi.org/10.1017/S0956792508007651
42. Kumar K, van Noorden TL, Pop IS. Effective dispersion equations for reactive flows involving free boundaries at the microscale. *Multiscale Model Simul*. 2011;9:29-58. https://doi.org/10.1137/100804553
43. Bringedal C, Berre I, Pop IS, Radu FA. A model for non-isothermal flow and mineral precipitation and dissolution in a thin strip. *J Comput Appl Math*. 2015;289:346-355. https://doi.org/10.1016/j.cam.2014.12.009
44. Huh C, Scriven LE. Hydrodynamic model of steady movement of a solid/liquid/fluid contact line. *J Colloid Interface Sci*. 1971;35:85-101.
45. Dussan V EB, Davis SH. On the motion of a fluid-fluid interface along a solid surface. *J Fluid Mech*. 1974;65:71-95. https://doi.org/10.1017/S0022112074001261
46. Dussan V EB. On the spreading of liquids on solid surfaces: static and dynamic contact lines. *Annu Rev Fluid Mech*. 1979;11:371-400. https://doi.org/10.1146/annurev.fl.11.010179.002103
47. Ren W, Weinan E. Boundary conditions for the moving contact line problem. *Phys Fluids*. 2007;19:022101. https://doi.org/10.1063/1.2646754
48. Bonn D, Eggers J, Indekeu J, Meunier J, Rolley E. Wetting and spreading. *Rev Mod Phys*. 2009;81:739-805. https://doi.org/10.1103/RevModPhys.81.739
49. Sui Y, Ding H, Spelt PD. Numerical simulations of flows with moving contact lines. *Annu Rev Fluid Mech*. 2014;46:97-119. https://doi.org/10.1146/annurev-fluid-010313-141338
50. Hocking LM. A moving fluid interface on a rough surface. *J Fluid Mech*. 1976;76:801-817.
51. Huh C, Mason SG. The steady movement of a liquid meniscus in a capillary tube. *J Fluid Mech*. 1977;81:401-419 https://doi.org/10.1017/S0022112077002134
52. de Gennes PG. Wetting: statics and dynamics. *Rev Mod Phys*. 1985;57:827-863. https://doi.org/10.1103/RevModPhys.57.827
53. Haley PJ, Miksis MJ. The effect of the contact line on droplet spreading. *J Fluid Mech*. 1991;223:57-81. https://doi.org/10.1017/S0022112091001337
54. Sheng P, Zhou M. Immiscible-fluid displacement: contact-line dynamics and the velocity-dependent capillary pressure. *Phys Rev A*. 1992;45:5694-5708. https://doi.org/10.1103/PhysRevA.45.5694
55. Ren W, Hu D, Weinan E. Continuum models for the contact line problem. *Phys Fluids*. 2010;22:102103. https://doi.org/10.1063/1.3501317
56. Greenspan HP. On the motion of a small viscous droplet that wets a surface. *J Fluid Mech*. 1978;84:125-143. https://doi.org/10.1017/S0022112078000075

57. Cox RG. The dynamics of the spreading of liquids on a solid surface. Part 1. Viscous flow. *J Fluid Mech*. 1986;168:169-194. https://doi.org/10.1017/S0022112086000332
58. Baer TA, Cairncross RA, Schunk R, Rao RR, Sackinger PA. A finite element method for free surface flows of incompressible fluids in three dimensions. Part II. Dynamic wetting lines. *Int J Numer Meth Fluids*. 2000;33:405-427. https://doi.org/10.1002/1097-0363(20000615)33:3⟨405::AID-FLD14⟩3.0.CO;2-4
59. Koplik J, Banavar JR, Willemsen JF. Molecular dynamics of Poiseuille flow and moving contact lines. *Phys Rev Lett*. 1988;60:1282-1285. https://doi.org/10.1103/PhysRevLett.60.1282
60. Koplik J, Banavar JR, Willemsen JF. Molecular dynamics of fluid flow at solid surfaces. *Phys. Fluids A Fluid Dyn*. 1989;1:781-794. https://doi.org/10.1063/1.857376
61. Thompson PA, Robbins MO. Simulations of contact-line motion: slip and the dynamic contact angle. *Phys Rev Lett*. 1989;63:766-769. https://doi.org/10.1103/PhysRevLett.63.766
62. Thompson PA, Brinckerhoff WB, Robbins MO. Microscopic studies of static and dynamic contact angles. *J Adhes Sci Technol*. 1993;7:535-554. https://doi.org/10.1163/156856193X00844
63. Koplik J, Banavar JR. Continuum deductions from molecular hydrodynamics. *Annu Rev Fluid Mech*. 1995;27:257-292. https://doi.org/10.1146/annurev.fl.27.010195.001353.
64. Jäger W, Mikelić A. On the roughness-induced effective boundary conditions for an incompressible viscous flow. *J Differ Equ*. 2001;170:96-122. https://doi.org/10.1006/jdeq.2000.3814
65. Maručić-Paloka E. Average of the Navier's law on the rapidly oscillating boundary. *J Math Anal Appl*. 2001;259:685-701. https://doi.org/10.1006/jmaa.2001.7505
66. Basson A, Gérard-Varet D. Wall laws for fluid flows at a boundary with random roughness. *Commun Pure Appl Math*. 2008;61:941-987. https://doi.org/10.1002/cpa.20237
67. Gérard-Varet D, Masmoudi N. Relevance of the slip condition for fluid flows near an irregular boundary. *Commun Math Phys*. 2010;295:99-137, https://doi.org/10.1007/s00220-009-0976-0
68. Blake TD. The physics of moving wetting lines. *J Colloid Interface Sci*. 2006;299:1-13. https://doi.org/10.1016/j.jcis.2006.03.051
69. Blake TD. Dynamic contact angles and wetting kinetics. In: Berg JC, ed. *Wettability*. New York: Marcel Dekker; 1993:251-309.
70. Ralston J, Popescu M, Sedev R. Dynamics of wetting from an experimental point of view. *Annu Rev Mater Res*. 2008;38:23-43. https://doi.org/10.1146/annurev.matsci.38.060407.130231
71. Voinov OV. Hydrodynamics of wetting. *Fluid Dyn*. 1976;11:714-721. https://doi.org/10.1007/BF01012963
72. Huh C, Mason SG. Effects of surface roughness on wetting (theoretical). *J Colloid Interface Sci*. 1977;60:11-38. https://doi.org/10.1016/0021-9797(77)90251-X
73. Blake TD, Haynes JM. Kinetics of liquid/liquid displacement. *J Colloid Interface Sci*. 1969;30:421-423. https://doi.org/10.1016/0021-9797(69)90411-1
74. Cherry BW, Holmes CM. Kinetics of wetting of surfaces by polymers. *J Colloid Interface Sci*. 1969;29:174-176. https://doi.org/10.1016/0021-9797(69)90367-1
75. Van Dyke M., *Perturbation Methods in Fluid Mechanics*. Annotated edition. Stanford, CA: Parabolic Press; 1975.
76. The MathWorks Inc. *MATLAB® Version 9.8.0.1417392 (R2020a)*. 2020. http://www.mathworks.com/products/matlab.html
77. Lunowa SB. AsymptoticThinStripMCLSolver – Solver for the asymptotic model of immiscible two-phase flow with moving contact line in a thin strip. 2020. https://github.com/s-lunowa/AsymptoticThinStripMCLSolver

How to cite this article: Lunowa SB, Bringedal C, Pop IS. On an averaged model for immiscible two-phase flow with surface tension and dynamic contact angle in a thin strip. *Stud Appl Math*. 2021;147:84–126. https://doi.org/10.1111/sapm.12376